

PAPER

Integrable turbulence generated from modulational instability of cnoidal waves

To cite this article: D S Agafontsev and V E Zakharov 2016 *Nonlinearity* **29** 3551

View the [article online](#) for updates and enhancements.

You may also like

- [Nanopteron solution of the Korteweg-de Vries equation](#)
Jianyong Wang, Xiaoyan Tang, Senyue Lou et al.
- [Complex PT-invariant cnoidal and hyperbolic solutions of several real nonlinear equations](#)
Avinash Khare and Avadh Saxena
- [Acoustic nonlinear periodic \(cnoidal\) waves and solitons in pair-ion plasmas](#)
T Kaladze, S Mahmood and Hafeez Ur-Rehman

Integrable turbulence generated from modulational instability of cnoidal waves

D S Agafontsev¹ and V E Zakharov^{1,2,3,4}

¹ P.P. Shirshov Institute of Oceanology, 36 Nakhimovsky prosp., Moscow 117218, Russia

² Department of Mathematics, University of Arizona, Tucson, AZ, 857201, USA

³ P.N. Lebedev Physical Institute, 53 Leninsky ave., 119991 Moscow, Russia

⁴ Novosibirsk State University, 2 Pirogova, 630090 Novosibirsk, Russia

E-mail: dmitrij@itp.ac.ru and zakharov@math.arizona.edu

Received 24 December 2015, revised 30 June 2016

Accepted for publication 2 September 2016

Published 30 September 2016



Recommended by Professor Koji Ohkitani

Abstract

We study numerically the nonlinear stage of the modulational instability (MI) of cnoidal waves in the framework of the focusing one-dimensional nonlinear Schrödinger (NLS) equation. Cnoidal waves are exact periodic solutions of the NLS equation which can be represented as the lattices of overlapping solitons. The MI of these lattices leads to the development of ‘integrable turbulence’ (Zakharov 2009 *Stud. Appl. Math.* **122** 219–34). We study the major characteristics of turbulence for the dn-branch of cnoidal waves and demonstrate how these characteristics depend on the degree of ‘overlapping’ between the solitons within the cnoidal wave.

Integrable turbulence, which develops from the MI of the dn-branch of cnoidal waves, asymptotically approaches its stationary state in an oscillatory way. During this process, kinetic and potential energies oscillate around their asymptotic values. The amplitudes of these oscillations decay with time as $t^{-\alpha}$, $1 < \alpha < 1.5$, the phases contain nonlinear phase shift decaying as $t^{-1/2}$, and the frequency of the oscillations is equal to the double maximal growth rate of the MI, $s = 2\gamma_{\max}$. In the asymptotic stationary state, the ratio of potential to kinetic energy is equal to -2 . The asymptotic PDF of the wave intensity is close to the exponential distribution for cnoidal waves with strong overlapping, and is significantly non-exponential for cnoidal waves with weak overlapping of the solitons. In the latter case, the dynamics of the system reduces to two-soliton collisions, which occur at an exponentially small rate and provide an up to two-fold increase in amplitude compared with the original cnoidal wave. For all cnoidal waves of the dn-branch, the rogue waves at the time of their maximal elevation have a quasi-rational profile similar to that of the Peregrine solution.

Keywords: modulational instability, integrable turbulence, rogue waves, numerical simulations, nonlinear Schrödinger equation

Mathematics Subject Classification numbers: 35Q55, 37K10, 37M05

(Some figures may appear in colour only in the online journal)

1. Introduction

The statistics of waves for different nonlinear systems has been intensively studied in recent years [1–10], especially since the first experimental observation of optical rogue waves [11]. Known previously for hydrodynamics [12–14], rogue waves are very large short pulses that may endanger marine navigation and optical communications. These pulses appear randomly from initially smooth waves and their statistics may significantly exceed those predicted by the approximations of random wave fields governed by linear equations.

Let us suppose that wave field ψ is a random superposition of a multitude of uncorrelated linear waves,

$$\psi(x) = \sum_k |\psi_k| e^{i(kx + \phi_k)}.$$

If phases ϕ_k are random and uncorrelated, the number of waves $\{k\}$ is large, and amplitudes $|\psi_k|$ fall under the conditions of the central limit theorem, then the real $\text{Re } \psi(x)$ and imaginary $\text{Im } \psi(x)$ parts are Gaussian-distributed, and the probability density function (PDF) for wave amplitude is the Rayleigh distribution [15],

$$\mathcal{P}_R(|\psi|) = \frac{2|\psi|}{\sigma^2} e^{-|\psi|^2/\sigma^2}. \quad (1)$$

Here, $\sigma^2 = \langle |\psi|^2 \rangle$ is the average square amplitude, and we use normalization for the PDF as $\int \mathcal{P}(|\psi|) d|\psi| = 1$. For convenience, below we study the PDFs for a normalized square amplitude $I = |\psi|^2 / \langle |\psi|^2 \rangle$, which has a meaning of relative intensity: the small waves correspond to $I \ll 1$, the moderate ones to $I \sim 1$, and the large ones to $I \gg 1$. Then, the Rayleigh PDF (1) takes the simple form

$$\mathcal{P}_R(I) = e^{-I}, \quad (2)$$

which we will call the exponential PDF (note that we called the same PDF Rayleigh in our previous paper [7]). If the evolution is governed by linear equations, then the superposition of the linear waves stays uncorrelated, and its PDF remains exponential (2). Nonlinear evolution may introduce a correlation, which in turn may lead to the enhanced appearance of large waves.

With a certain degree of accuracy, many physical systems can be described by completely integrable (nonlinear) mathematical models. In comparison with nonintegrable models, the corresponding integrable equations demonstrate significantly different statistical properties [16–18]. The new emerging field of nonlinear science which studies these properties was introduced in 2009 by Zakharov [16] as ‘integrable turbulence’. The one-dimensional nonlinear Schrödinger (NLS) equation of focusing type,

$$i\psi_t + \psi_{xx} + |\psi|^2\psi = 0, \quad (3)$$

is paid special attention in these studies, since it is a simple mathematical model suitable for the description of rogue waves in optics and hydrodynamics [12–14]. The simplest ‘condensate’ solution $\psi = e^{it}$ of equation (3) is modulationally unstable, and the development of this instability from an initially small perturbation may lead to the appearance of rogue waves [12, 13].

However, as we demonstrated in our previous paper [7], for the NLS equation and in the scenario of the modulational instability (MI) of the condensate, the PDF of the wave intensity, averaged over realizations of the initial perturbation, does not exceed the exponential PDF significantly (2). The development of MI leads to integrable turbulence, which asymptotically approaches its stationary state in an oscillatory way. The PDF in this state is exponential (2). During evolution toward the stationary state, the PDF significantly deviates from (2), however it does not exceed the exponential PDF by more than a few times.

Another physically relevant scenario of the emergence of rogue waves in the framework of the NLS equation was studied in [8, 10] for incoherent waves as initial conditions (see also the earlier studies [19–21] with similar results for the long crested water waves of the JONSWAP spectrum, and also a similar study for the defocusing NLS equation [6]). For incoherent waves, integrable turbulence quickly reaches its stationary state, in which the tail of the PDF at high intensities exceeds exponential distribution (2) by orders of magnitude.

The fact that the different initial conditions of these studies lead to entirely different results is not surprising: integrable systems ‘remember’ their initial condition through the conservation of an infinite series of invariants (integrals of motion). These invariants are different for different types of initial conditions, and thus the stationary states and the evolution toward them are different too. However, so far there has been no explanation why in one case integrable turbulence approaches its stationary state for a very long time and the probability of the appearance of rogue waves is small, while in the other case the stationary state is reached very quickly and rogue waves appear much more frequently.

In this publication we study one more scenario, in which integrable turbulence develops from the MI of cnoidal waves. Cnoidal waves are exact periodic solutions of the NLS equation (3), essentially depending on two parameters ω_0 and ω_1 , which we will call real and imaginary half-periods respectively. There are dn- and cn-branches of such solutions. The dn-branch of cnoidal waves can be written as

$$\psi_{\text{dn}}(x, t) = e^{i\Omega t} \sqrt{2} \nu \operatorname{dn}(\nu x; s^2), \quad (4)$$

where $\operatorname{dn}(x; s^2)$ is the corresponding Jacobi elliptic function and Ω , ν and s are specific values defined by the half-periods ω_0 and ω_1 (see appendix A for more details). The solutions (4) are periodic with the period $2\omega_0$, and at $t = 0$ they are purely real and positive, $\psi_{\text{dn}}(x, 0) > 0$; an example of one such solution with half-periods $\omega_0 = \pi$ and $\omega_1 = 1.6$ is shown in figure 1(a). The cn-branch of cnoidal waves can be written as

$$\psi_{\text{cn}}(x, t) = e^{i\Omega t} \sqrt{2} s\nu \operatorname{cn}(\nu x; s^2), \quad (5)$$

where $\operatorname{cn}(x; s^2)$ is the corresponding Jacobi elliptic function. These solutions are periodic with the period $4\omega_0$, and at $t = 0$ they are purely real and change their sign periodically with x . An example of such a solution for the same half-periods $\omega_0 = \pi$ and $\omega_1 = 1.6$ is shown in figure 1(b).

As described in appendix A, both types of cnoidal waves can be viewed as infinite lattices of overlapping NLS solitons,

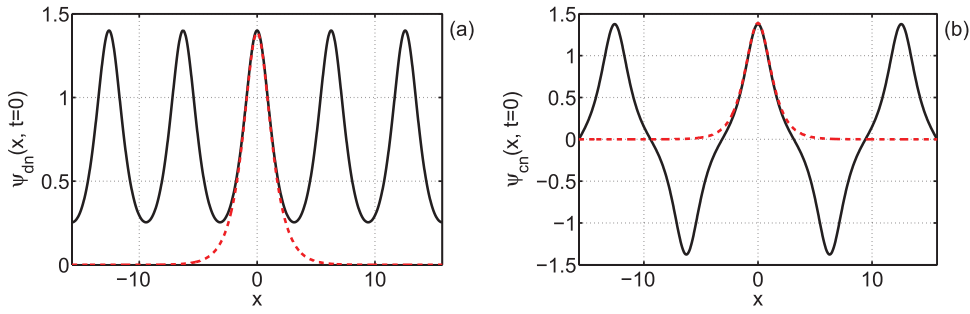


Figure 1. The cnoidal waves of (a) the dn-branch (4) and (b) the cn-branch (5) with $\omega_0 = \pi$, $\omega_1 = 1.6$, at $t = 0$ when they are purely real, $\text{Im } \psi_{\text{dn}}(x, 0) = \text{Im } \psi_{\text{cn}}(x, 0) = 0$. The dashed red lines show the soliton (6) with $\lambda = \pi/2\omega_1$.

$$\psi_s(x, t) = e^{i\lambda^2 t} \frac{\sqrt{2} \lambda}{\cosh \lambda x}, \quad \lambda = \pi/2\omega_1, \tag{6}$$

with the width of the solitons proportional to ω_1 and the distance between them equal to $2\omega_0$. For weak ‘overlapping’ between the solitons $\omega_1/\omega_0 \ll 1$, cnoidal waves transform into the arithmetic sum of NLS solitons,

$$\psi(x, t) \rightarrow e^{i\lambda^2 t} \sum_{m=-\infty}^{+\infty} \frac{(-1)^{\varrho m} \sqrt{2} \lambda}{\cosh \lambda(x - 2m\omega_0)}, \tag{7}$$

where $\varrho = 0$ for the dn-branch and $\varrho = 1$ for the cn-branch. For strong ‘overlapping’ $\omega_1/\omega_0 \gg 1$, the cnoidal waves of the dn-branch transform into condensate,

$$\psi_{\text{dn}}(x, t) \rightarrow \sqrt{2} \kappa e^{2i\kappa^2 t}, \tag{8}$$

while the cnoidal waves of the cn-branch transform into sinusoidal waves with an exponentially small amplitude,

$$\psi_{\text{cn}}(x, t) \rightarrow [4\sqrt{2} \kappa \exp(-\kappa \omega_1)] e^{-i\kappa^2 t} \cos(\kappa x), \tag{9}$$

where $\kappa = \pi/2\omega_0$. Both branches of cnoidal waves are modulationally unstable. For the dn-branch, the maximal growth rate of the MI was found in [22],

$$\gamma_{\text{max}} = 2\nu (e_1 - e_2)^{1/2}. \tag{10}$$

For a fixed ω_0 , this relation is exponentially small for small ω_1 , monotonically increases with ω_1 , and approaches $2\kappa^2$ as $\omega_1 \rightarrow +\infty$. To the authors’ knowledge, γ_{max} has not been found for the cn-branch so far.

In this paper, we study the statistical properties of the MI for the dn-branch of cnoidal waves only. It will be more convenient to work with the stationary variants of the cnoidal waves,

$$\Psi_{\text{dn}}(x) = \sqrt{2} \nu \text{dn}(\nu x; s^2), \tag{11}$$

which are solutions of the slightly modified NLS equation

$$i\Psi_t - \Omega \Psi + \Psi_{xx} + |\Psi|^2 \Psi = 0, \tag{12}$$

obtained from equation (3) after gauge transformation $\psi = e^{i\Omega t}\Psi$. To study the statistical properties of the MI of cnoidal waves (11), one has to solve equation (12) with the initial conditions

$$\Psi|_{t=0} = \Psi_{\text{dn}}(x) + \epsilon(x), \quad |\epsilon(x)| \ll |\Psi_{\text{dn}}(x)|, \tag{13}$$

and average the results over different realizations of the initial noise $\epsilon(x)$. Without loss of generality, we will consider cnoidal waves with a real half-period $\omega_0 = \pi$ only. Indeed, the NLS equation can be scaled $t \rightarrow \chi t$, $x \rightarrow \eta x$ and $\Psi \rightarrow \mu \Psi$ using three independent parameters χ , η and μ . Two of these parameters can be used to scale the dispersion and nonlinearity coefficients to unity, while the last parameter can be used to scale ω_0 to π . Then, in the limits (8) and (9) the constant $\kappa = \pi/2\omega_0$ is equal to 1/2, and the cnoidal waves from the dn-branch transform into a condensate with the amplitude $1/\sqrt{2}$ as $\omega_1 \rightarrow +\infty$.

Formally, the problem (12) with initial conditions (13) could be solved analytically, as any periodic solution of the NLS equation can be expressed explicitly in terms of the Jacobi θ -functions over a certain hyperbolic curve, see e.g. [23–25]. However, to study the general case of MI, we have to use an initial noise $\epsilon(x)$ with a very large number of excited modes, which also makes the genus of the curve very large (for the present study we use at least 10^4 harmonics). It is unrealistic so far to follow this evolution with exact analytical methods.

Therefore, we rely completely on numerical experiments, solving the NLS equation (12) in the box $x \in [-L/2, L/2]$ with a periodic boundary. Integrability implies the conservation of an infinite series of integrals of motion. The first three of these invariants are wave action,

$$N = \frac{1}{L} \int_{-L/2}^{L/2} |\Psi(x, t)|^2 dx, \tag{14}$$

momentum,

$$P = \frac{i}{2L} \int_{-L/2}^{L/2} (\Psi_x^* \Psi - \Psi_x \Psi^*) dx, \tag{15}$$

and total energy,

$$E = H_d + H_4, \quad H_d = \frac{1}{L} \int_{-L/2}^{L/2} |\Psi_x|^2 dx, \quad H_4 = -\frac{1}{2L} \int_{-L/2}^{L/2} |\Psi|^4 dx. \tag{16}$$

Here, H_d is kinetic and H_4 is potential energy. The other invariants,

$$c_n[\Psi] = \frac{1}{L} \int_{-L/2}^{L/2} \phi_n dx, \tag{17}$$

can be calculated using the following recurrent series of equations [24]:

$$\phi_{n+1} = \Psi \frac{\partial}{\partial x} \left(\frac{\phi_n}{\Psi} \right) + \sum_{l+m=n} \phi_l \phi_m, \quad \phi_1 = |\Psi|^2/2. \tag{18}$$

Our method of numerical simulations conserves the first ten invariants very well.

The general motivation of our study is to improve our understanding of integrable turbulence. In [7, 8, 10], two cases of integrable turbulence were studied with the initial condensate and incoherent wave conditions respectively. With the help of scaling transformations, the problem of the MI of the condensate renormalizes to equation (3) and the condensate $\psi = e^{it}$ for all dispersion and nonlinearity coefficients as well as for all condensates [7]. Thus, except for the noise, this problem does not depend on any free parameters. The evolution of the

incoherent wave in formulation [8, 10] essentially depends on one free parameter, and the initial potential to kinetic energy ratio can be used as such. However, so far an extensive study of how integrable turbulence depends on this parameter has not been performed. Cnoidal waves are a class of modulationally unstable solutions of the focusing NLS equation. For a fixed $\omega_0 = \pi$, the properties of these solutions essentially depend on one parameter ω_1 , which determines the degree of ‘overlapping’ between the solitons within the cnoidal wave (see appendix A). Thus, we can expect that integrable turbulence generated from the MI of these waves will also significantly depend on ω_1 .

Cnoidal waves with small ω_1 are very close to the arithmetic sum of equally spaced very thin and high NLS solitons (7). Turbulence generated from the MI of such waves should be close to soliton turbulence in an integrable system (for soliton turbulence in nonintegrable systems, see e.g. [26, 27]). For large ω_1 we should obtain results similar to those for initial condensate conditions [7], since such cnoidal waves are close to condensate (8). Changing ω_1 , we can study how the properties of integrable turbulence transform from those for integrable soliton turbulence to those for the MI of the condensate.

As we demonstrate in this publication, many of the presented facts do not have a theoretical explanation so far. We hope that the results of our study, together with the studies of the condensate and incoherent wave initial conditions [7, 8, 10] will help in the development of a consistent theory of integrable turbulence. Our study also has a practical meaning. Solitons (6) are proposed as information bits in optical communications, which are generally described very well by the NLS equation. To increase the communication bit-rate, it is necessary to pack these solitons sufficiently close to each other (see e.g. [28, 29]). Our study shows how often large waves may appear in some of the regimes of these communications.

In this publication we consider the following ensemble-averaged characteristics of the turbulence: (1) kinetic $\langle H_d(t) \rangle$ and potential $\langle H_4(t) \rangle$ energies, (2) wave-action spectrum $S_k(t)$ and spatial correlation function $g(x, t)$, and (3) moments of amplitude $M^{(n)}(t)$ and the PDF for relative intensity $\mathcal{P}(I, t)$. Here and below $\langle \dots \rangle$ stands for the arithmetic average across an ensemble of initial conditions. We define the wave-action spectrum as

$$S_k(t) = \langle |\Psi_k(t)|^2 \rangle, \tag{19}$$

where $\Psi_k(t)$ is the Fourier transform of $\Psi(x, t)$,

$$\Psi_k(t) = \mathcal{F}[\Psi(x, t)] = \frac{1}{L} \int_{-L/2}^{L/2} \Psi(x, t) e^{-ikx} dx, \tag{20}$$

$$\Psi(x, t) = \mathcal{F}^{-1}[\Psi_k(t)] = \sum_k \Psi_k(t) e^{ikx}. \tag{21}$$

Here, $k = 2\pi m/L$ is the wavenumber and $m \in \mathbb{Z}$ is the integer. The wave-action spectrum is the spectral density of the wave action $\langle N \rangle$,

$$\langle N \rangle = \langle |\Psi|^2 \rangle = \sum_k S_k(t), \tag{22}$$

where $\langle |\Psi|^2 \rangle$ is an ensemble and space average of the square amplitude. The spatial correlation function,

$$g(x, t) = \left\langle \frac{1}{L} \int_{-L/2}^{L/2} \Psi(y, t) \Psi^*(y - x, t) dy \right\rangle / \langle N \rangle, \tag{23}$$

is connected to the wave-action spectrum as

$$g(x, t) = \mathcal{F}^{-1}[S_k(t)] / \langle N \rangle. \tag{24}$$

Due to this definition, at $x = 0$ the correlation function is always fixed to unity, $g(0, t) = 1$.

Moments of amplitude,

$$M^{(n)}(t) = \left\langle \frac{1}{L} \int_{-L/2}^{+L/2} |\Psi(x, t)|^n dx \right\rangle, \tag{25}$$

are connected to the PDF $\mathcal{P}(|\Psi|, t)$ of the wave amplitude $|\Psi|$ as

$$M^{(n)}(t) = \int_0^{+\infty} |\Psi|^n \mathcal{P}(|\Psi|, t) d|\Psi|. \tag{26}$$

The second moment coincides with the wave action $M^{(2)}(t) = \langle |\Psi|^2 \rangle = \langle N \rangle$, and thus does not change with time. The potential energy is connected to the fourth moment as $\langle H_4(t) \rangle = -M^{(4)}(t)/2$ (see e.g. [30] where this relation is extensively exploited). For the exponential PDF (2) the moments would be equal to

$$M_E^{(n)} = \langle N \rangle^{n/2} \Gamma(n/2 + 1), \tag{27}$$

where $\Gamma(m)$ is a gamma-function. Below we will call the moments (27) exponential moments.

In the present study, we demonstrate that after the development of the MI, all of the considered characteristics of the resulting integrable turbulence evolve with time in an oscillatory way, approaching their asymptotics at late times. Hence, one can say that the MI of cnoidal waves leads to integrable turbulence, which asymptotically approaches in an oscillatory way its stationary state defined by infinite series of invariants (17) and (18). The numerical simulations presented below show that during evolution toward a stationary state, the kinetic $\langle H_d(t) \rangle$ and potential $\langle H_4(t) \rangle$ energies, as well as the moments $M^{(n)}(t)$, oscillate with time around their asymptotic values. The amplitudes of these oscillations decay with time as $t^{-\alpha}$, $1 < \alpha < 1.5$, the phases contain nonlinear phase shift decaying as $t^{-1/2}$, and the frequency of the oscillations is equal to the double maximal growth rate of the MI, $s = 2\gamma_{\max}$. Very similar oscillations are present in the condensate case [7]. Remarkably, the asymptotic potential to kinetic energy ratio turns out to be equal to $Q_A = \langle H_4 \rangle / \langle H_d \rangle = -2$ for all cnoidal waves of the dn-branch. The wave-action spectrum, spatial correlation function and the PDF evolve coherently with the oscillations of potential energy, so that at the local maximums and minimums of $|\langle H_4(t) \rangle|$ their evolution changes to roughly the opposite. We describe the evolution of these functions in detail in sections 3 and 4 of this paper.

For cnoidal waves with small ω_1 , we observe that the wave field remains close to a collection of solitons (6) at all times with different positions and phases, even when the system is close to the asymptotic state. Thus, the turbulence generated from the MI of such cnoidal waves is indeed close to the integrable soliton turbulence of very thin and high solitons (6). In its asymptotic stationary state, the PDF is significantly non-exponential and the dynamics of the system reduces to two-soliton collisions. These collisions provide an increase of up to two-fold in amplitude and occur at an exponentially small rate $\propto e^{-\pi\omega_0/\omega_1}$. The potential to kinetic energy ratio $Q(t) = \langle H_4(t) \rangle / \langle H_d(t) \rangle$ remains very close to -2 at all times, the same as for a singular soliton (6). For cnoidal waves with a large ω_1 , the asymptotic PDF coincides with the exponential PDF (2).

The properties of the integrable turbulence change gradually with ω_1 . The MI of cnoidal waves with ‘intermediate’ ω_1 leads to turbulence with ‘intermediate’ properties between the two limits $\omega_1 \rightarrow 0$ and $\omega_1 \rightarrow +\infty$. All the rogue waves that we examined, for all the cnoidal

waves that we studied, have a quasi-rational profile at the time of their maximal elevation similar to that of the Peregrine solution [31, 32] of the NLS equation.

The paper is organized as follows. In section 2 we describe the numerical methods used in our study. In section 3 we consider the general properties of integrable turbulence that develop from the MI of the dn-branch of cnoidal waves, for the example of one cnoidal wave with a fixed imaginary half-period ω_1 . The dependence of these properties on ω_1 is described in section 4. The final section 5 contains the conclusions. In appendix A we explain the cnoidal wave solutions in more detail, and in appendix B we demonstrate how the MI develops on the background of three cnoidal waves with $\omega_1 = 0.8$ (weak overlapping), $\omega_1 = 1.6$ (moderate overlapping) and $\omega_1 = 5$ (strong overlapping).

2. Numerical methods

We integrate equation (12) numerically in the box $x \in [-L/2, L/2]$ with a periodic boundary. Typically, we use $L = 256\pi$ and integrate equation (12) up to the final time $t = 200$ —although in some cases we use larger boxes and/or integration times. Large integration times $t \geq 200$ are necessary, since for our initial conditions the evolution close to the asymptotic stationary state is a very long process. Large boxes L are necessary, because we encounter recurrence starting from some time T , which might be connected to the Fermi–Pasta–Ulam (FPU) phenomenon [33, 34]. The time of this recurrence increases linearly with the box size [7], $T \propto L$. To avoid it influencing our results, we used sufficiently large boxes L and additionally ran our experiments on boxes twice as large $2L$ to ensure that our results did not depend quantitatively on L .

As in [7], we use the Runge–Kutta fourth-order method with adaptive change of the spatial grid size Δx and a Fourier interpolation of the solution between the grids. To avoid the appearance of numerical instabilities, the time step Δt changes with Δx as $\Delta t = h\Delta x^2$, $h \leq 0.1$. The simulations conserve the first ten invariants (17) and (18) with an accuracy better than 10^{-6} . Note, that we measure relative errors for the integrals $c_n[\Psi]$ with odd orders $\text{mod}(n, 2) = 1$ and absolute errors for integrals with even orders $\text{mod}(n, 2) = 0$, since for unperturbed cnoidal waves (11) the latter ones are zeroth. The first three invariants—wave action (14), momentum (15) and total energy (16)—are conserved with accuracy better than 10^{-10} .

We start the simulations on the grid with $M = 16\,384$ nodes (or proportionally larger when using larger boxes L) from the initial conditions (13) where the real half-period is fixed to $\omega_0 = \pi$. For each of the studied cnoidal waves characterized by the imaginary half-period ω_1 , we average our results across an ensemble of 1000 random realizations of the initial noise $\epsilon(x)$. We use noise which is statistically homogeneous in space

$$\epsilon(x) = A_0 \left(\frac{\sqrt{8\pi}}{\theta L} \right)^{1/2} \sum_k e^{-k^2/\theta^2 + i\xi_k + ikx}, \quad (28)$$

where A_0 is the noise amplitude, $k = 2\pi m/L$ is the wavenumber, $m \in \mathbb{Z}$ is the integer, θ is the noise width in k -space and ξ_k are the arbitrary phases for each k and each noise realization within the ensemble of initial conditions. As shown in [7], in x -space the average square amplitude of such noise is $\langle |\epsilon|^2 \rangle = A_0^2$. Below, we will present our results for initial noise with parameters $A_0 = 10^{-5}$ and $\theta = 5$. We performed experiments with other parameters A_0 and θ too, but did not find a significant difference. We also checked our statistical results against the size of the ensembles and parameters of our numerical scheme, and found no difference either.

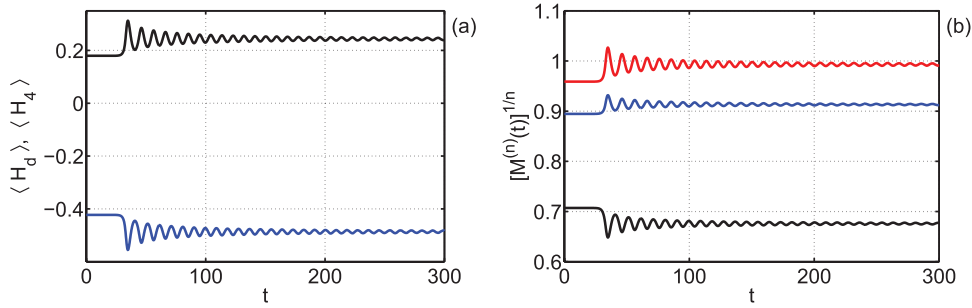


Figure 2. (a) The evolution of ensemble averaged kinetic $\langle H_d(t) \rangle$ (black) and potential $\langle H_4(t) \rangle$ (blue) energies. In the asymptotic stationary state, their ratio is equal to $Q_A = \langle H_4 \rangle / \langle H_d \rangle = -2$. (b) The evolution of moments $M^{(1)}(t)$ (black), $[M^{(3)}(t)]^{1/3}$ (blue) and $[M^{(4)}(t)]^{1/4}$ (red).

3. Evolution toward the asymptotic stationary state

The results of this section are illustrated by the example of the MI of the cnoidal wave (11) with $\omega_1 = 1.6$, which is an ‘intermediate’ cnoidal wave between the two limits $\omega_1 \rightarrow 0$ and $\omega_1 \rightarrow +\infty$, see figure 1(a). The corresponding numerical simulations were carried out in the box $L = 1024\pi$ up to the final time $t = 2000$. The cnoidal waves with other ω_1 give qualitatively similar results; the dependence on ω_1 will be considered in more detail in section 4.

The MI of the cnoidal wave (11) with $\omega_1 = 1.6$ has a maximal increment (10) $\gamma_{\max} = 0.356$ and reaches its nonlinear stage at about $t \sim 30$ (see figure B1 in appendix B). Then, all the statistical characteristics that we studied start to evolve in an oscillatory way, approaching their asymptotics at late times. An example of such evolution for the kinetic $\langle H_d(t) \rangle$ and potential $\langle H_4(t) \rangle$ energies, and also moments $M^{(n)}(t)$, is shown in figures 2(a) and (b). Thus, one can conclude that after the development of the MI, the system asymptotically approaches its stationary state in an oscillatory way, which in turn is defined by an infinite series of invariants (17) and (18). In order to determine the characteristics of this asymptotic state (e.g. the kinetic and potential energies, the moments, the PDF, etc), we average the corresponding functions both across the ensemble of initial conditions and over the time close to the asymptotic state $t \in [1800, 2000]$.

The potential to kinetic energy ratio $Q(t) = \langle H_4(t) \rangle / \langle H_d(t) \rangle$ changes from $Q(t) = -2.3$ at $t = 0$ to $Q_A = -2$ in the asymptotic stationary state. The same asymptotic energy ratio $Q_A = -2$ is observed for the MI of the condensate. Following [7], we determine that in the nonlinear stage of the MI the evolution of moments $M^{(n)}(t)$ is very well approximated by the functions

$$M^{(n)}(t) \approx M_A^{(n)} + [p/t^\alpha] \sin(st + q/\sqrt{t} + \Phi_0), \tag{29}$$

where $M_A^{(n)}$ are asymptotic moments and α, p, s, q, Φ_0 are constants (different for different moments). An example of such an approximation for the first moment $M^{(1)}(t)$ is shown in figure 3. The kinetic $\langle H_d(t) \rangle$ and potential $\langle H_4(t) \rangle$ energies also oscillate according to (29) due to the relation $\langle H_4(t) \rangle = -M^{(4)}(t)/2$ and conservation of total energy; the second moment does not oscillate since $M^{(2)}(t) = \langle N \rangle$. The potential energy $\langle H_4(t) \rangle$ and the first moment $M^{(1)}(t)$ oscillate in-phase, with parameters $s = 0.71, q = 74.6$ and $\Phi_0 = -1.23$. The kinetic energy

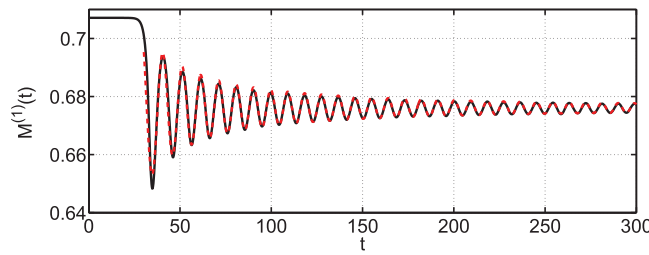


Figure 3. The evolution of moment $M^{(1)}(t)$ (solid black) and its fit by function $f(t) = M_A^{(1)} + [pt^\alpha] \sin(st + q/\sqrt{t} + \Phi_0)$ with parameters $M_A^{(1)} = 0.676$, $\alpha = 1.23$, $p = 1.82$, $s = 0.71$, $q = 74.6$, $\Phi_0 = -1.23$ (dashed red).

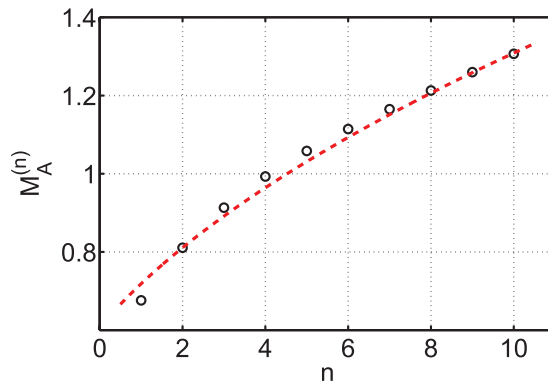


Figure 4. The asymptotic moments $[M_A^{(n)}]^{1/n}$, $n = 1, \dots, 10$ (black circles) and exponential moments $[M_E^{(n)}]^{1/n}$ (27) (dashed red line).

$\langle H_d(t) \rangle$ and higher moments $M^{(n)}(t)$, $n \geq 3$, oscillate with the parameters $s = 0.71$, $q = 74.6$ and $\Phi_0 = 1.91$, which are in-phase with each other and exactly anti-phase with the potential energy and the first moment. The amplitudes of these oscillations decay with time by the power law $\propto t^{-\alpha}$, with the exponent decreasing from $\alpha = 1.23$ for the first moment to $\alpha = 1.08$ for the tenth moment. The asymptotic moments $M_A^{(n)}$ differ slightly from the exponential moments (27), as shown in figure 4.

The wave-action spectrum of the original cnoidal wave represents a collection of peaks at integer wavenumbers $k_0 \in \mathbb{Z}$. Since for all the cnoidal waves (11) the following equality is valid,

$$\Psi_{k=0} = \frac{1}{L} \int_{-L/2}^{L/2} \Psi_{\text{dn}}(x) dx = \pi/\sqrt{2} \omega_0,$$

the peak at the zeroth harmonic is equal to $S_0 = |\Psi_{k=0}|^2 = 0.5$. The peaks at nonzero wavenumbers $|k_0| > 0$ nearly decay exponentially with $|k_0|$. The spatial correlation function for the unperturbed cnoidal wave is periodic with the same period 2π as the original cnoidal wave, everywhere positive $g(x) > 0$, takes maximal values $\max g(x) = g(0) = 1$ at $x = 2\pi m$, $m \in \mathbb{Z}$, and minimal values at $x = 2\pi(m + 1/2)$.

In the linear stage of MI, the wave-action spectrum $S_k(t)$ at the non-integer wavenumbers starts to rise; the fastest increase is observed close to the half-integer wavenumbers, figure 5(a). At this time, the spatial correlation function $g(x, t)$ does not change visibly, figure 5(b). At the

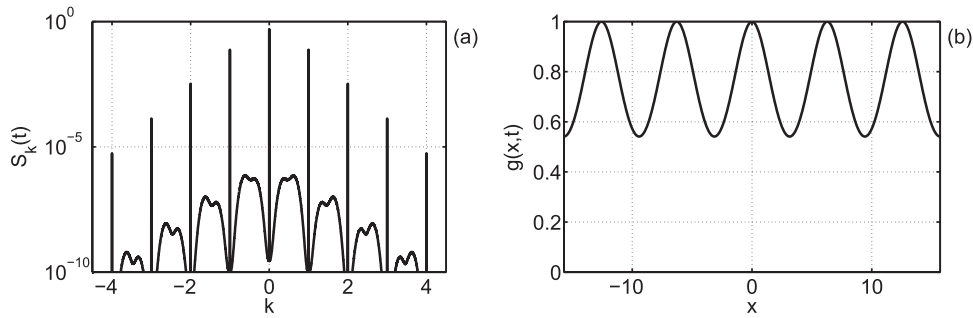


Figure 5. The wave-action spectrum $S_k(t)$ (a) and spatial correlation function $g(x,t)$ (b) in the linear stage of the MI at $t = 20$.

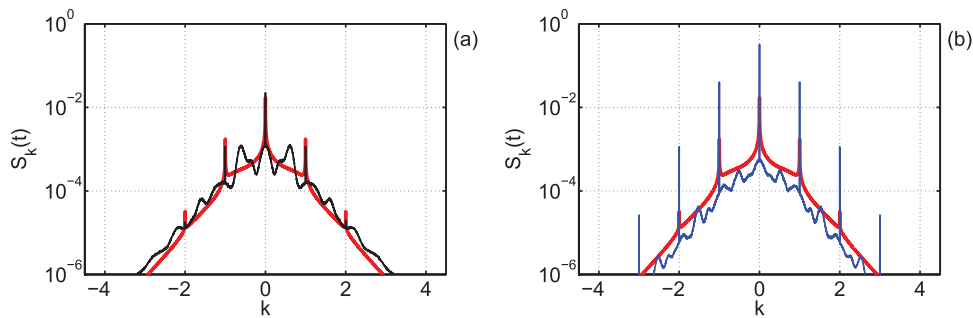


Figure 6. The wave-action spectrum $S_k(t)$: (a) at the first local maximum of the potential energy modulus $|\langle H_4(t) \rangle|$ at $t = 34.8$ (black) and (b) at the first local minimum of $|\langle H_4(t) \rangle|$ at $t = 40.6$ (blue). The asymptotic wave-action spectrum is shown in thick red.

nonlinear stage, the spectrum and the correlation function evolve with time in an oscillatory way approaching their asymptotics at late times. The ‘turning points’ for this oscillatory evolution—i.e. the points in time when their evolution changes to roughly the opposite—coincide with time when the moments $M^{(n)}(t)$, and also the kinetic $\langle H_d(t) \rangle$ and potential $\langle H_4(t) \rangle$ energies, take their maximal or minimal values. For definiteness, below we will refer to such points in time for the example of local maximums and minimums of the potential energy modulus $|\langle H_4(t) \rangle|$. At the local maximums of $|\langle H_4(t) \rangle|$, the peaks at the integer wavenumbers k_0 in the spectrum $S_k(t)$ are the smallest and the rest of the spectrum is maximally excited, figures 6(a) and 7, while the correlation function $g(x,t)$ takes (locally in time) minimal values at $|x| > 0$, figures 8(a) and (b). At the local minimums of $|\langle H_4(t) \rangle|$, the peaks at k_0 are the largest and the rest of the spectrum is minimally excited, figures 6(b) and 7, while the correlation function takes (locally in time) maximal values at $|x| > 0$, figures 8(a) and (b). Thus, one can say that during the evolution toward the asymptotic state, the wave action is being ‘pumped’ in an oscillatory way between the peaks at integer wavenumbers and the rest of the spectrum, while the correlation function ‘forms’ its tails at large lengths.

The asymptotic wave-action spectrum decays exponentially at large k as $\propto e^{-\rho|k|}$, $\rho = 1.15$, and contains peaks at $k_0 = 0, \pm 1, \pm 2, \pm 3$, figure 9(a). Contrary to the original cnoidal wave, these peaks now occupy not only the integer wavenumbers k_0 , but also small regions around them. One such region around the zeroth harmonic is shown in figure 9(b). Similarly to the condensate case [7], the spectrum in this region behaves by the power law $S_k \propto |k|^{-\beta}$, with almost

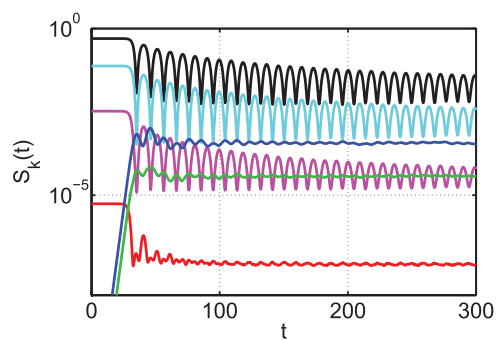


Figure 7. The time dependence of the wave-action spectrum $S_k(t)$ at $k = 0$ (black), $k = 0.5$ (blue), $k = 1$ (cyan), $k = 1.5$ (green), $k = 2$ (pink) and $k = 4$ (red).

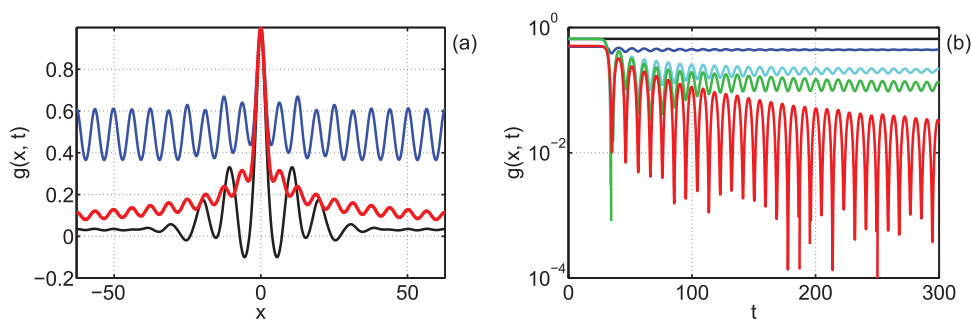


Figure 8. (a) The spatial correlation function $g(x, t)$ at the first local maximum of the potential energy modulus $|\langle H_4(t) \rangle|$ at $t = 34.8$ (black) and the first local minimum of $|\langle H_4(t) \rangle|$ at $t = 40.6$ (blue). The asymptotic correlation function is shown in thick red. (b) The time dependence of the spatial correlation function $g(x, t)$ at $x = 0$ (black), $x = \pi/2$ (blue), $x = 2\pi$ (cyan), $x = 8\pi$ (green), and at the border of the computational box $x = L/2$ (red).

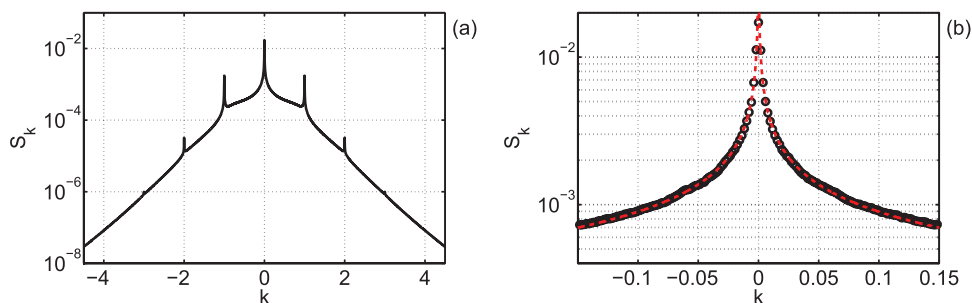


Figure 9. (a) The asymptotic wave-action spectrum S_k . (b) The asymptotic wave-action spectrum S_k in the vicinity of $k = 0$ (black circles) and its fit by function $f(k) = b|k|^{-\beta}$, $b = 2.2 \times 10^{-4}$, $\beta = 0.61$ (dashed red). At $k = 0$, the asymptotic spectrum is finite, $S_0 = 1.72 \times 10^{-2}$. Graphs (a) and (b) contain about 4600 and 150 harmonics respectively, with the distance between them $\Delta k = 2\pi/L = 1/512$.

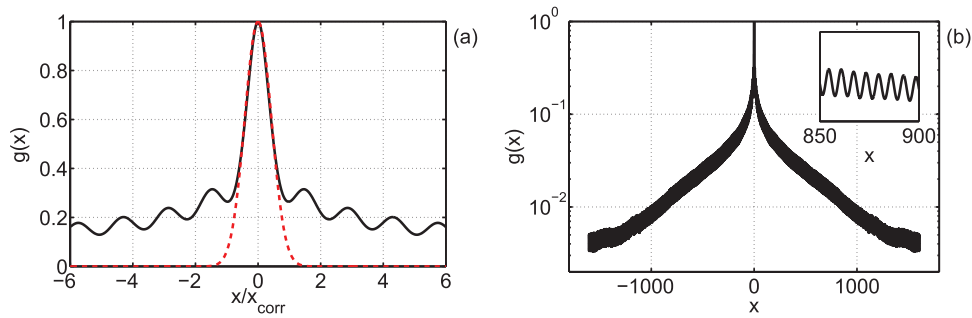


Figure 10. The asymptotic spatial correlation function $g(x)$ versus x/x_{corr} , $x_{\text{corr}} = 4.4$ (a) and x (b). The dashed red line in graph (a) shows the Gaussian distribution (30), the inset in graph (b) shows the oscillations of $g(x)$ with the period 2π .

the same exponent $\beta = 0.61$. At $k = 0$, the asymptotic spectrum is finite, $S_0 = 1.72 \times 10^{-2}$. The other peaks in the spectrum also exhibit power-law behaviour, $S_k \propto |k - k_0|^{-\beta}$, with different exponents β for different peaks ($\beta = 0.56$ for $k_0 = \pm 1$, $\beta = 0.25$ for $k_0 = \pm 2$, and peaks at $k_0 = \pm 3$ are too small for analysis); at k_0 the spectrum is finite. The power-law behaviour of the peaks means that the wave action is concentrated in the corresponding modes. The peak at the zeroth harmonic is sufficiently wide, with the power-law expanding in the modes $|k| \leq \delta k$, $\delta k = 0.15$. The other peaks are much narrower, with $\delta k = 0.02$ for $k_0 = \pm 1$ and $\delta k = 0.01$ for $k_0 = \pm 2$. The modes $|k - k_0| \leq \delta k$ contain about 39% of all wave action $\langle N \rangle$ for the zeroth harmonic $k_0 = 0$, about 4% for $k_0 = \pm 1$, and less than 0.1% for $k_0 = \pm 2$; in total, the seven peaks contain about 43% of all wave action $\langle N \rangle$. The modes $|k| \leq 0.15$, which contain most of this wave action, have extremely large scales $\ell \gg 2\pi$ in the physical space, and can be called quasi-condensate [7].

The asymptotic spatial correlation function is shown in figures 10(a) and (b). Its characteristic scale, defined as full width at half maximum, is $x_{\text{corr}} = 4.4$. At small lengths $|x| < x_{\text{corr}}/2$ the correlation function is well-approximated by the Gaussian

$$g(x) \approx \exp\left[-\ln 2 \left(\frac{2x}{x_{\text{corr}}}\right)^2\right]. \tag{30}$$

At large lengths $|x| \gg x_{\text{corr}}$ it decays close to exponentially and in an oscillatory way, as shown in figure 10(b); the period of these oscillations is equal to 2π .

As shown in figure 4, the asymptotic moments $M_A^{(n)}$ differ from the exponential moments (27). This means that the PDF $\mathcal{P}_A(I)$ in the asymptotic state must differ from the exponential PDF (2). This is indeed the case, as shown in figure 11(a). The asymptotic PDF exceeds the exponential PDF for relative intensities $I < 0.22$, $I \in [1.9, 4.2]$ and $I \in [8.7, 14.4]$. According to the rogue waves criterion $|\Psi|^2 > 8\langle |\Psi|^2 \rangle$ (see e.g. [7, 12, 13]), or $I > 8$, only the last region contains rogue waves. In this region $I \in [8.7, 14.4]$ the asymptotic PDF exceeds the exponential PDF by about 2.5 times the maximum at $I = 12$. Note, that in the region $I \in [0, 2]$ the asymptotic PDF turns out to be very close to the initial PDF $\mathcal{P}(I, t)$ at $t = 0$, as shown in the inset of figure 11(a).

After the development of the MI, the PDF $\mathcal{P}(I, t)$ evolves with time in an oscillatory way approaching the asymptotic PDF at late times, as shown in figures 11(b), 12(a) and (b). This

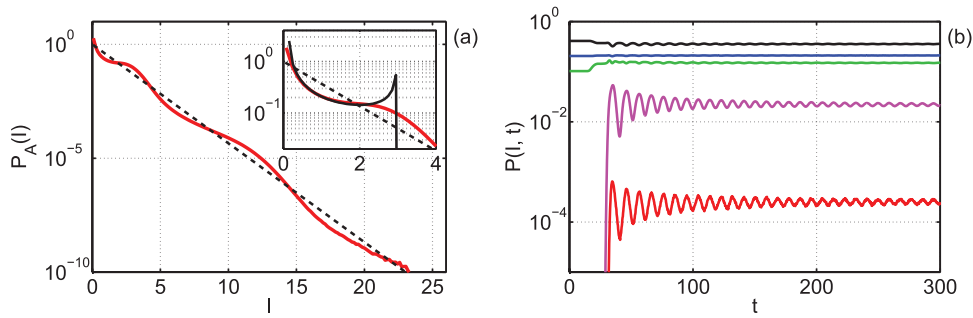


Figure 11. (a) The asymptotic PDF $\mathcal{P}_A(I)$ (thick red) and exponential PDF (2) (dashed black). The inset shows the same PDFs and also the initial PDF $\mathcal{P}(I, t)$ at $t = 0$ (black solid line). (b) The time dependence of the PDF $\mathcal{P}(I, t)$ at different relative intensities $I = 0.5$ (black), $I = 1$ (blue), $I = 2$ (green), $I = 4$ (pink), $I = 8$ (red).

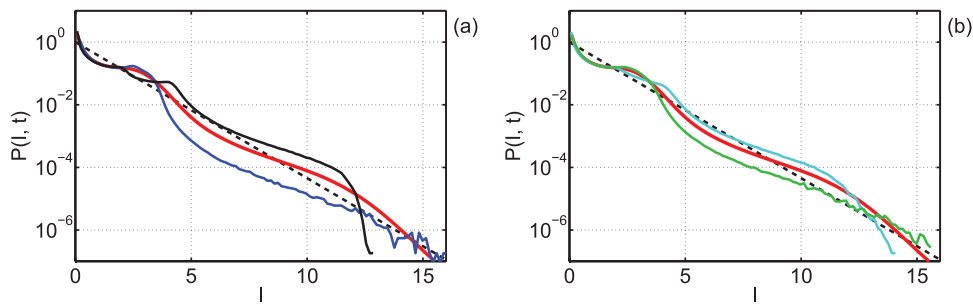


Figure 12. The PDF $\mathcal{P}(I, t)$ at different times corresponding to the first several potential energy modulus $|\langle H_4(t) \rangle|$ extremums: (a) at $t = 34.8$ (black, first local maximum of $|\langle H_4(t) \rangle|$), $t = 40.6$ (blue, first local minimum) and (b) at $t = 46.2$ (cyan, second local maximum), $t = 51.4$ (green, second local minimum). The thick red line shows the asymptotic PDF $\mathcal{P}_A(I)$, the dashed black line is the exponential PDF (2).

evolution is similar to that of a wave-action spectrum and spatial correlation function, with the same ‘turning points’ coinciding with local maximums and minimums of $|\langle H_4(t) \rangle|$. At the local maximums of $|\langle H_4(t) \rangle|$ and for sufficiently large intensities $4 \lesssim I \lesssim 12$, the PDF $\mathcal{P}(I, t)$ takes (locally in time) maximal values, figures 12(a) and (b). At the local minimums of $|\langle H_4(t) \rangle|$ the PDF takes (locally in time) minimal values for the same region of intensities. A maximal excess of the PDF $\mathcal{P}(I, t)$ over the exponential PDF (2) by about six times is observed at the first local maximum of $|\langle H_4(t) \rangle|$ at $t = 34.8$ for a relative intensity of $I = 11.5$.

Figures 13 and 14 show two rogue wave events—a typical one and the largest detected one respectively. The rogue wave in figure 13 had a duration of $\Delta T \sim 1$ and reached a maximal amplitude $\max|\Psi| = 2.8$ at $t_0 = 34.9$, which is close to the first local maximum of $|\langle H_4(t) \rangle|$ at $t = 34.8$. With the average square amplitude $\langle |\Psi|^2 \rangle = 0.66$, the crest of this wave corresponds to the relative intensity $I = 12$. The largest detected wave shown in figure 14 had a duration of $\Delta T \sim 0.5$ and reached a maximal amplitude of $\max|\Psi| = 4.4$ at $t = 1361.4$, which is sufficiently close to the asymptotic stationary state. The crest of this wave corresponds to a relative intensity of $I = 29$.

We examined several hundred of the rogue waves detected in our experiments, and found that all of them have a quasi-rational profile at the time of their maximal elevation, similar to

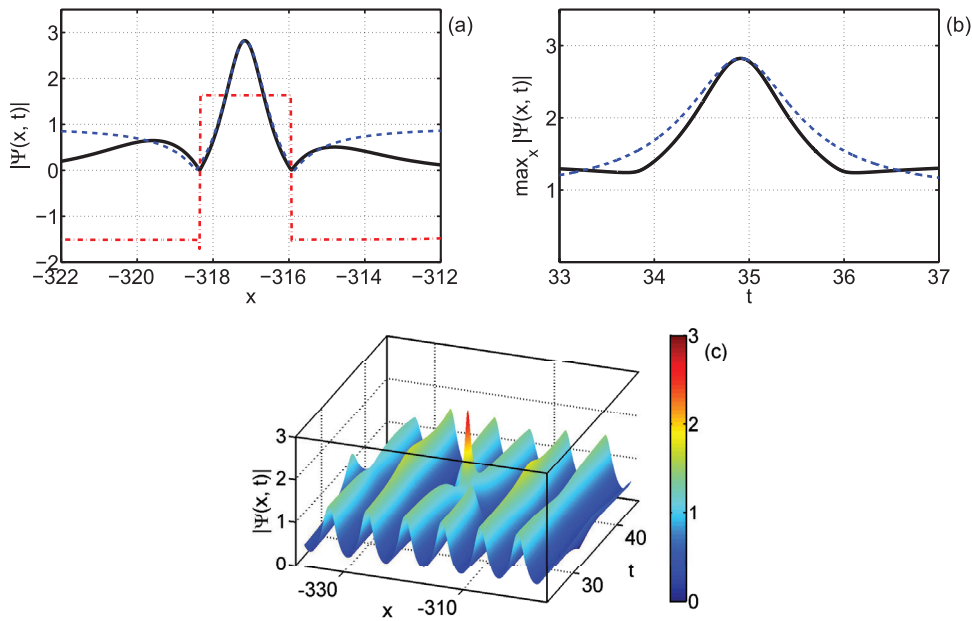


Figure 13. (a) The space distribution of amplitude $|\Psi(x, t_0)|$ (solid black) and phase $\arg \Psi(x, t_0)$ (dashed-dotted red) for a typical rogue wave at $t_0 = 38.9$ of its maximal elevation. The dashed blue line is fit by the Peregrine solution (32) with $A = -0.94$, $x_0 = -317.2$. (b) The time evolution of the maximal amplitude for a rogue wave (solid black) and a Peregrine solution (33) (dashed blue). (c) The space-time representation of amplitude $|\Psi(x, t)|$ near the rogue wave event.

that of the Peregrine solution [31, 32] (see the similar results in [10] for incoherent wave initial conditions and in [9] for the generalized NLS equation accounting for six-wave interactions, pumping and dumping terms). The Peregrine solution is localized in the space and time algebraic solution of the NLS equation (3),

$$\psi_P(x, t) = e^{it} \left[1 - \frac{4(1 + 2it)}{1 + 2x^2 + 4t^2} \right]. \tag{31}$$

It is easy to see that $A \psi_P(X, T)$, where $X = |A|(x - x_0)$ and $T = |A|^2(t - t_0)$, is also a solution of the NLS equation, which becomes maximal at $x = x_0$ and $t = t_0$. Figures 13(a) and 14(a) show the similarity of the rogue wave profile (at the time of its maximal elevation $t = t_0$) with that of the Peregrine solution,

$$|\Psi(x, t_0)| \approx A \psi_P(X, 0) = A \left[1 - \frac{4}{1 + 2|A|^2(x - x_0)^2} \right]. \tag{32}$$

Note, that the phase of rogue waves $\arg \Psi(x, t_0)$ is almost constant near the amplitude maximum, as is the case for the Peregrine solution at the time of its maximal elevation. Moreover, for one realization from the ensemble of initial conditions we checked all the waves that exceeded the maximal amplitude of the original cnoidal wave by 1.5 times or more. At the time of their maximal elevation, all such waves are well approximated in space by the ansatz (32). However, the time evolution of the maximal amplitude $\max_x |\Psi(x, t)|$ for large waves is different from that,

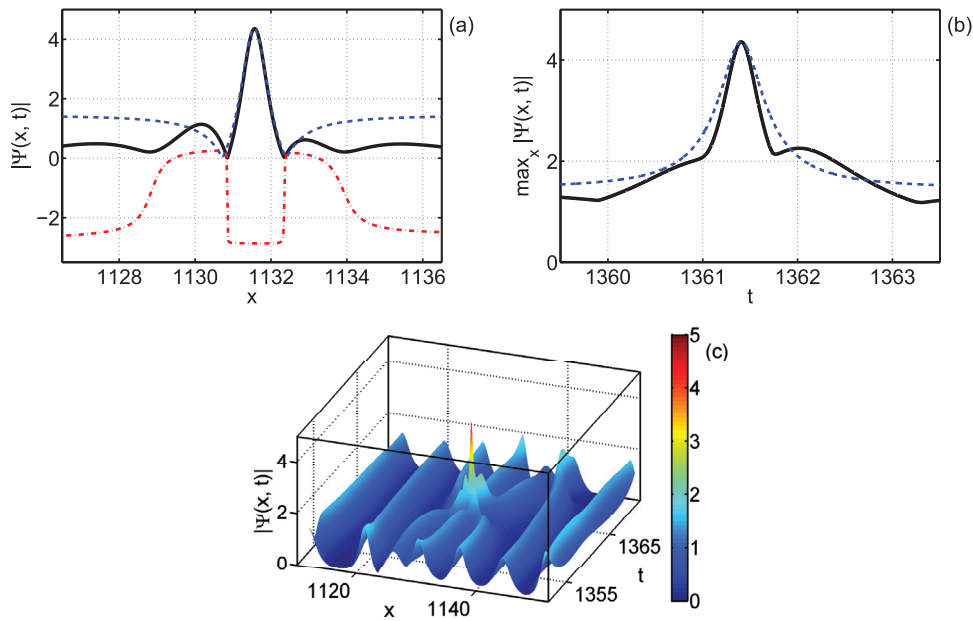


Figure 14. (a) The space distribution of amplitude $|\Psi(x, t_0)|$ (solid black) and phase $\arg \Psi(x, t_0)$ (dashed-dotted red) for the largest detected rogue wave at $t_0 = 1361.4$ of its maximal elevation. The dashed blue line is fit by the Peregrine solution (32) with $A = -1.46$, $x_0 = 1131.6$. (b) The time evolution of the maximal amplitude for the rogue wave (solid black) and Peregrine solution (33) (dashed blue). (c) The space-time representation of amplitude $|\Psi(x, t)|$ near the rogue wave event.

$$A |\psi_p(0, T)| = A \left| 1 - 4 \frac{1 + 2i|A|^2(t - t_0)}{1 + 4|A|^4(t - t_0)^2} \right|, \tag{33}$$

for the Peregrine solution; see examples in figures 13(b) and 14(b).

The phase of those rogue waves which appear near the first several local maximums of $|\langle H_4(t) \rangle|$ is very close to $\arg \Psi \approx \pi/2 + \pi(m - 1)$, where m is the local maximum index number (i.e. $\arg \Psi \approx \pi/2$ for the first local maximum at $t = 34.8$, $\arg \Psi \approx 3\pi/2$, for the second local maximum at $t = 46.2$, etc). The phase of those rogue waves which appear near the first several local minimums of $|\langle H_4(t) \rangle|$ is very close to $\arg \Psi \approx \pi + \pi(m - 1)$, where m is the local minimum index number. We observe such behaviour for about the ten first local maximums and minimums of the potential energy modulus $|\langle H_4(t) \rangle|$. We checked this fact by direct observation (see e.g. figure 13(a)) and also by measuring the PDFs for the real and imaginary parts of the wave field Ψ . The same ‘rotation of phase’ is present for the condensate case [7] too.

As shown in figures 13(c) and 14(c), the rogue waves in these figures look like collisions of two and three pulses respectively. In terms of the recent study of rogue waves on cnoidal wave backgrounds [35], the wave in figure 13 might be the ‘concentrated’ cnoidal rogue wave, while the wave in figure 14 might be the ‘fused’ second-order cnoidal rogue wave. There is also another possibility, which is that the waves in figures 13 and 14 are the collisions of breathers that decompose from ‘superregular’ solitonic solutions on the cnoidal wave background [36]. Similar solutions on the condensate background were recently found theoretically [37] and observed experimentally [38]. Such solutions on the cnoidal wave background should

decompose to breathers, and subsequent collisions of these breathers may lead to the almost algebraic behaviour of the resulting pulse at the time of its maximal elevation (see e.g. [39] of how this may happen for Akhmediev breathers). We plan to study the question of the origin of rogue waves in more detail in another publication.

4. Dependence on cnoidal wave parameters

In this section, we describe the dependence of integrable turbulence on cnoidal wave parameters, namely the imaginary half-period ω_1 , which determines the ‘overlapping’ between the solitons within the cnoidal wave. For this purpose we repeated the numerical experiment of section 3 for another ten cnoidal waves (11) with imaginary half-periods from $\omega_1 = 0.8$ to $\omega_1 = 5$, which have maximal increments of the MI (10) γ_{\max} from 0.065 to 0.5 respectively. These experiments were carried out in the box $L = 256\pi$ up to the final time from $t = 200$ (for $\omega_1 = 5$) to $t = 1000$ (for $\omega_1 = 0.8$). The properties of the generated integrable turbulence turned out to be qualitatively similar to that discussed in section 3. Therefore, below we will focus mainly on the distinctions in the properties of the turbulence for different initial cnoidal waves.

For small ω_1 , the cnoidal waves are very close to the arithmetic sum of singular solitons (7), as demonstrated by the example in figure 15(a) for $\omega_1 = 0.8$. After the development of the MI from such waves (see figure B2 in appendix B), the wave field remains close to a composition of singular solitons (6) with different phases and positions, even after a very long time when the system is close to the asymptotic stationary state, figure 16. Moreover, the positions of these singular solitons remain generally very close to the positions of the ‘solitons’ of the original cnoidal wave. Note, that the phase $\arg \Psi(x, t)$ stays almost constant on the solitons and randomly jumps between them. Therefore, the turbulence generated from cnoidal waves with small ω_1 transforms into soliton turbulence in the integrable system. The potential to kinetic energy ratio $Q(t)$ for such turbulence remains very close to -2 at all times, figure 17(a)—the same as for a singular NLS soliton (6).

The development of the MI from cnoidal waves with a large ω_1 is similar to that for the condensate (see figure B3 in appendix B), and these waves are themselves close to the condensate (8), figure 15(b). The initial energy ratio for such cnoidal waves is large, $-Q(0) \gg 1$, see figure 18(a), and the asymptotic ratio $Q_A = -2$ is the same as for the condensate case [7], see figure 17(b). Moreover, the asymptotic energy ratio is equal to $Q_A = -2$ for all cnoidal waves of the dn-branch that we studied, though the nature of this beautiful relation remains unclear to us so far, figure 18(a).

In the nonlinear stage of the MI, the kinetic $\langle H_2(t) \rangle$ and potential $\langle H_4(t) \rangle$ energies, as well as the moments $M^{(n)}(t)$, approach their asymptotic values in an oscillatory way. These oscillations are very well approximated by the functions (29) for all the cnoidal waves that we studied. However, for $\omega_1 \leq 1$ we were only able to check this for the first four moments, since the oscillations for such cnoidal waves are very small—compare figures 17(a) and (b). The exponent α for the power-law decay $\propto t^{-\alpha}$ of the amplitude of these oscillations is different for different cnoidal waves and moments $M^{(n)}(t)$, and stays in the range $1 < \alpha < 1.5$. It turns out that the frequency of the oscillations is equal to the double maximal growth rate of the MI (10), $s = 2\gamma_{\max}$, figure 18(b). For small ω_1 the maximal growth rate (10) is exponentially small [22],

$$\gamma_{\max} \rightarrow 8 \left(\frac{\pi}{\omega_1} \right)^2 \exp \left(-\frac{\pi\omega_0}{\omega_1} \right), \quad (34)$$

and for large ω_1 it approaches that of the condensate (8) with an amplitude of $1/\sqrt{2}$,

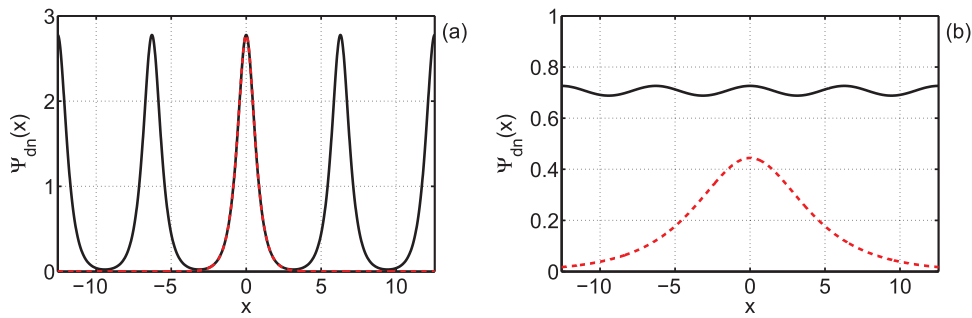


Figure 15. Cnoidal waves (11) with $\omega_1 = 0.8$ (a) and $\omega_1 = 5$ (b) at $t = 0$. The dashed red lines show solitons (6) with $\lambda = \pi/2\omega_1$.

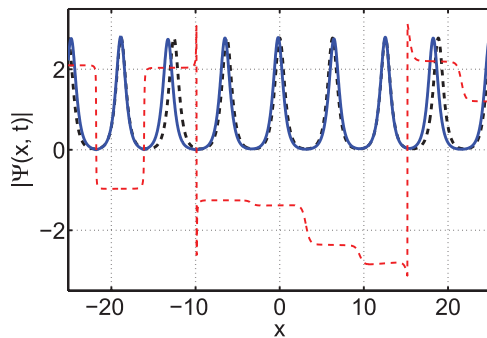


Figure 16. The amplitude $|\Psi(x, t)|$ for one of the realizations of the initial conditions for the cnoidal wave (11) with $\omega_1 = 0.8$: at $t = 0$ (dashed black) and close to the asymptotic state at $t = 1000$ (solid blue). The dashed red line shows the phase $\arg \Psi(x, t)$ at $t = 1000$.

$$\gamma_{\max} \rightarrow 1/2. \tag{35}$$

The same relation between the frequency of the oscillations and the maximal growth rate of the MI is valid for the condensate case [7] too. More study is necessary to clarify the nature of this beautiful phenomenon.

The asymptotic wave-action spectrum decays exponentially at large wavenumbers, $S_k \propto e^{-\rho|k|}$. The exponent ρ increases with ω_1 , so that for larger ω_1 the spectrum is narrower, see figures 19(a) and (b). For $\omega_1 = 5$ we obtain $\rho = 1.42$, which after the scaling transformations quantitatively corresponds to the condensate case [7]. Only one peak at the zeroth harmonic ‘survives’ in the asymptotic spectrum for cnoidal waves with large ω_1 , while for small ω_1 many of such peaks at integer wavenumbers k_0 remain. The spectrum in these peaks behaves by the power law, $S_k \propto |k - k_0|^{-\beta}$, with different exponents $\beta > 0$ for different cnoidal waves and peaks $|k_0|$. The peaks accumulate about 40% of all wave action $\langle N \rangle$ for all the cnoidal waves that we studied. For large ω_1 this fraction of wave action is concentrated in quasi-condensate modes $|k| \leq \delta k$, $\delta k \sim 0.1$, only. For small ω_1 the peak at the zeroth harmonic becomes narrower and the other peaks become wider, so that their widths and the fractions of wave action concentrated in them become comparable. Thus, the quasi-condensate is replaced by a ‘quasi-cnoidal wave’—a collection of power-law peaks at the same positions where the peaks of the original cnoidal wave were situated.

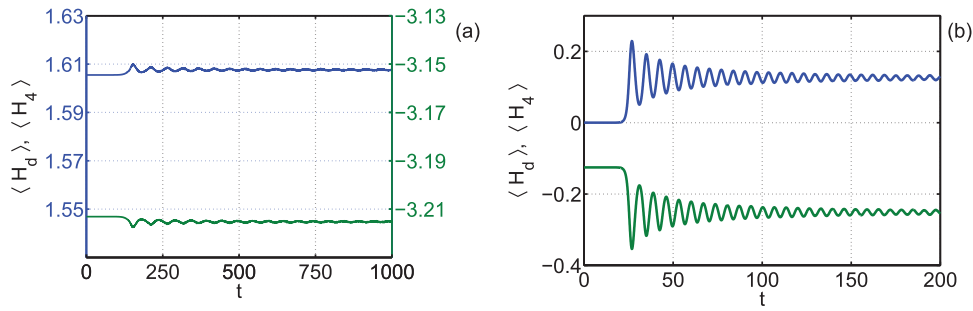


Figure 17. The evolution of ensemble averaged kinetic $\langle H_d(t) \rangle$ (blue) and potential $\langle H_4(t) \rangle$ (green) energies for cnoidal waves with $\omega_1 = 0.8$ (a) and $\omega_1 = 5$ (b). Note the difference in scales between graphs (a) and (b), and also the different OY-axis (left for $\langle H_d(t) \rangle$ and right for $\langle H_4(t) \rangle$) in graph (a). In the asymptotic stationary state the energy ratio is equal to $Q_A = \langle H_4 \rangle / \langle H_d \rangle = -2$ for both cnoidal waves.

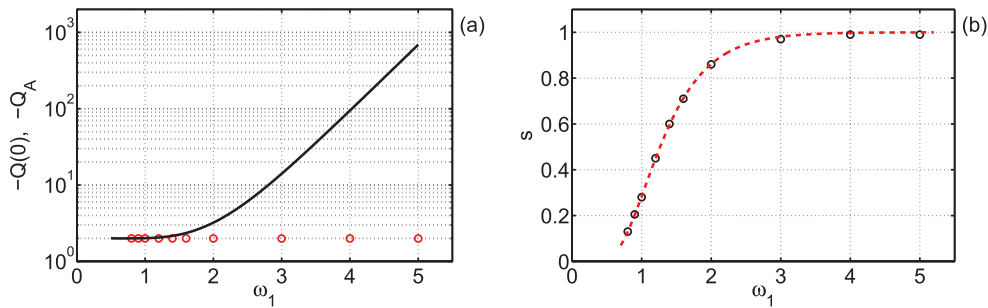


Figure 18. (a) The initial $-Q(0)$ (solid black line) and asymptotic $-Q_A$ (red circles) potential to kinetic energy ratio, versus ω_1 . (b) The frequency of the oscillations s for different cnoidal waves (black circles), versus ω_1 . The dashed red line shows the double maximal growth rate of the MI $2\gamma_{\max}$, see equation (10), for these cnoidal waves.

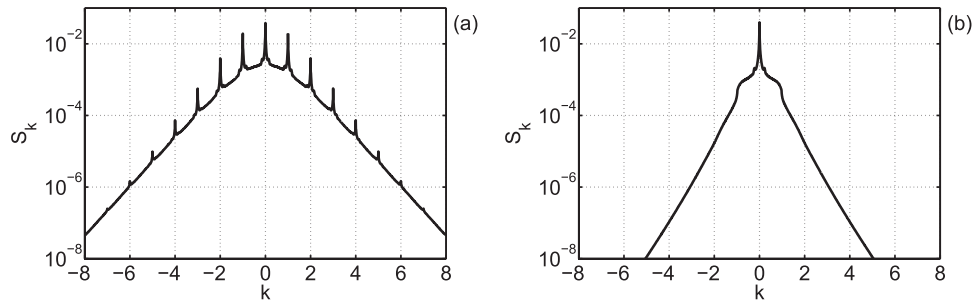


Figure 19. The asymptotic wave-action spectrum S_k for cnoidal waves with $\omega_1 = 0.8$ (a) and $\omega_1 = 5$ (b). Small irregularities at the bases of the peaks disappear at later times. At large k the spectrum decays exponentially $S_k \propto e^{-\rho|k|}$ with $\rho = 0.81$ for $\omega_1 = 0.8$ and $\rho = 1.42$ for $\omega_1 = 5$.

At small lengths $|x| < x_{\text{corr}}/2$ the asymptotic spatial correlation function is well approximated by the Gaussian (30). Its full width at half maximum increases with ω_1 ; for $\omega_1 = 0.8$ we measure $x_{\text{corr}} = 2.2$ and for $\omega_1 = 5$ we find $x_{\text{corr}} = 5.6$. After the scaling transformations, the

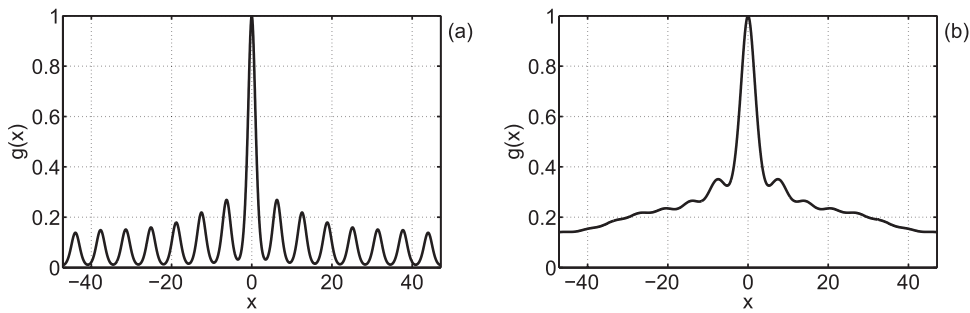


Figure 20. Asymptotic spatial correlation function $g(x)$ for cnoidal waves with $\omega_1 = 0.8$ (a) and $\omega_1 = 5$ (b). In graph (a) the period of the oscillations is equal to 2π .

latter value almost coincides with that of the condensate case [7]. For small ω_1 the asymptotic correlation function decays with $|x|$ in an oscillatory way; the period of these oscillations is equal to 2π , figure 20(a). The oscillations become more pronounced for cnoidal waves with smaller ω_1 . We think that their amplitude decays with $|x|$ exponentially, in a similar way to figure 10(b) for $\omega_1 = 1.6$. However, for cnoidal waves with sufficiently small $\omega_1 \leq 1.2$ we cannot check this hypothesis with our computational resources. These oscillations with period 2π are connected with the peaks at nonzero integer wavenumbers $|k_0| > 0$ in the asymptotic spectrum, since the oscillations change drastically if we ‘erase’ the spectrum near the corresponding modes. For large ω_1 both the peaks in the asymptotic spectrum at $|k_0| > 0$ and the oscillations of the asymptotic spatial correlation function disappear, figures 19(b) and 20(b), and the correlation function decay is inversely proportional to $|x|$, $g(x) \propto |x|^{-1}$, as for the condensate case [7].

For small ω_1 the asymptotic PDF is significantly non-exponential, figure 21(a). In particular, for $\omega_1 = 0.8$ the maximal deviation from the exponential PDF (2) is observed at $I = 24.2$, where the asymptotic PDF $\mathcal{P}_A(I) \approx 7.8 \times 10^{-9}$ exceeds the exponential PDF by about 250 times. However, for these ω_1 the typical deviation of square amplitude $|\Psi|^2$ is significantly larger than its mean value $\langle |\Psi|^2 \rangle$, see e.g. figure 16. Therefore, it is also instructive to measure the PDF $\mathcal{P}(I_m, t)$ for a square amplitude $I_m = |\Psi|^2 / \max |\Psi_{dn}|^2$, renormalized to the maximal amplitude of the original cnoidal wave $\max |\Psi_{dn}|$. In this case, $I_m = 1$ corresponds to the maximal amplitude $|\Psi| = \max |\Psi_{dn}|$ of the initial cnoidal wave, $I_m = 4$ corresponds to a two-fold increase in amplitude $|\Psi| = 2 \max |\Psi_{dn}|$, and so on. As shown in figure 22(a), for small ω_1 the asymptotic PDF $\mathcal{P}_A(I_m)$ decreases sharply at $I_m = 1$ and $I_m = 4$, and ends almost exactly at $I_m = 4$. Figure 21(a) also demonstrates that the PDF almost does not change with time at $I_m \in [0, 1]$ (which corresponds to $I \in [0, 6]$ in the figure), and the asymptotic PDF almost coincides in this region with the the initial PDF at $t = 0$. These facts corroborate our observation that after the development of the MI from cnoidal waves with small ω_1 , the wave field remains close to a composition of singular solitons (6) at all times. Then, the first part of the PDF $I_m \in [0, 1]$ in figure 22(a) represents this composition of solitons, and the second part $I_m \in [1, 4]$ corresponds to very rare two-soliton collisions. During these collisions, the wave amplitude exceeds the maximal amplitude of the original cnoidal wave by a maximum of twice the amount.

The rate of such collisions should be proportional to the maximal growth rate of the MI γ_{\max} , which is exponentially small (34) for small ω_1 . As shown in figure 22(b), in the region of two-soliton collisions $I_m \in [1, 4]$ the renormalized asymptotic PDFs $\mathcal{P}_A(I_m) \times e^{\pi\omega_0/\omega_1}$ coincide almost exactly for sufficiently small ω_1 (this coincidence is worse if we compare $\mathcal{P}_A(I_m)/\gamma_{\max}$). Thus, for small ω_1 the rate of two-soliton collisions and the probability of the occurrence of

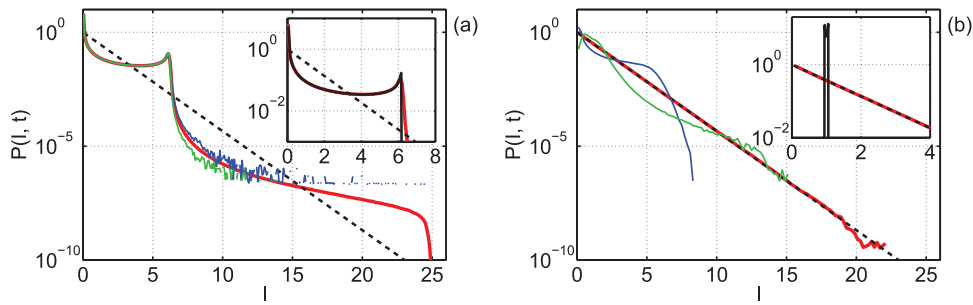


Figure 21. The asymptotic PDF $\mathcal{P}_A(I)$ (thick red) and exponential PDF (2) (dashed black) for cnoidal waves with $\omega_1 = 0.8$ (a) and $\omega_1 = 5$ (b). Solid black lines in the insets show the corresponding initial PDFs $\mathcal{P}(I, t)$ at $t = 0$. The blue lines are the PDFs at the first local maximum of potential energy modulus $|\langle H_4(t) \rangle|$ at $t = 151.4$ (a) and $t = 26.85$ (b), the green lines are the PDFs at the first local minimum of $|\langle H_4(t) \rangle|$ at $t = 179.8$ (a) and $t = 31.05$ (b). Note that the asymptotic PDFs $\mathcal{P}_A(I)$ are additionally averaged over time close to the asymptotic stationary state, which allows us to measure these PDFs for larger relative intensities I than the PDFs at specific times $\mathcal{P}(I, t)$.

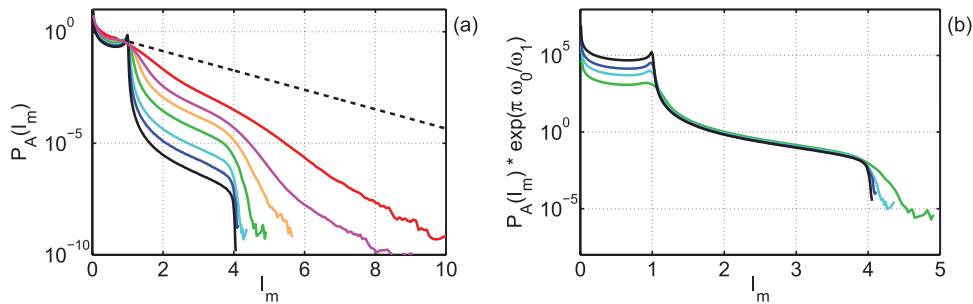


Figure 22. The asymptotic PDF $\mathcal{P}_A(I_m)$ (a) and renormalized asymptotic PDF $\mathcal{P}_A(I_m) \times e^{\pi\omega_0/\omega_1}$ (b) for the renormalized square amplitude $I_m = |\Psi|^2 / \max|\Psi_{dn}|^2$: for $\omega_1 = 0.8$ (black), $\omega_1 = 0.9$ (blue), $\omega_1 = 1$ (cyan), $\omega_1 = 1.2$ (green), $\omega_1 = 1.4$ (yellow), $\omega_1 = 1.6$ (pink) and $\omega_1 = 2$ (red). Here, $\max|\Psi_{dn}|$ is the maximal amplitude of the original cnoidal wave.

waves that are twice as large as the original cnoidal wave are proportional to $e^{-\pi\omega_0/\omega_1}$, which is an exponentially small value. We think that three-soliton collisions should also be present on the PDF, but they are extremely rare and we do not detect them in our experiments. We observe the first rogue waves that look like three-pulse collisions starting from the cnoidal wave with $\omega_1 = 1.6$, figure 14(c).

For sufficiently large ω_1 , the PDF in the asymptotic stationary state coincides with the exponential PDF (2), figure 21(b). This coincidence is already almost exact from $\omega_1 = 3$. In the nonlinear stage of the MI, the PDF may deviate significantly from the exponential PDF. If we limit ourselves to rogue waves $I > 8$ only, then for the cnoidal wave with $\omega_1 = 5$ the maximal excess of about 2.5 times of the PDF $\mathcal{P}(I, t)$ over the exponential PDF is achieved at the first local minimum of the potential energy modulus $|\langle H_4(t) \rangle|$ at $t = 31.05$ and for a relative intensity $I = 12.5$. These results coincide with that of the condensate case [7].

Thus, for cnoidal waves with $\omega_1 \gtrsim 1.5$ the probability of the occurrence of rogue waves is not significantly larger than for a random wave field governed by linear equations. For

$\omega_1 \lesssim 1.5$ the wave field is close to a collection of singular solitons that rarely interact with each other. The amplitude of these solitons is already significantly larger than the mean amplitude $(\langle |\Psi|^2 \rangle)^{1/2}$. Therefore, it is no surprise that rogue waves with an intensity much larger than the mean may appear in this system with probabilities exceeding the exponential PDF (2) by orders of magnitude. However, the amplitude of these rogue waves almost never exceeds the double maximal amplitude of the original cnoidal wave.

For each of the ten studied cnoidal waves ω_1 , we examined several of the largest rogue waves detected in our experiments. For $\omega_1 \geq 1.6$ many of these rogue waves look like three-pulse collisions, similar to that in figure 14(c), while for $\omega_1 < 1.6$ all of these rogue waves look like two-pulse collisions similar to that in figure 13(c). For the first several extremums of the potential energy modulus, the phases of the rogue waves are close to $\arg \Psi \approx \pi/2 + \pi(m-1)$ for local maximums and $\arg \Psi \approx \pi + \pi(m-1)$ for local minimums of $|\langle H_4(t) \rangle|$, where m is the local maximum or local minimum index number respectively. Also, we studied the evolution of one realization from an ensemble of initial conditions for each of the ten cnoidal waves ω_1 , examining all waves that exceed the maximal amplitude of the original cnoidal wave by 1.5 times or more at any time. For $\omega_1 = 0.8$ we found 14 such events in the time interval $t \in [0, 1000]$, and for $\omega_1 = 5$, more than 1500 events in the interval $t \in [0, 200]$. All these waves, and also all of the largest rogue waves generated from the entire ensembles of initial conditions, have a quasi-rational profile similar to that of the Peregrine solution (32) at the time of their maximal elevation; see examples in figures 13(a) and 14(a). The time evolution of the maximal amplitude for these waves differs from that of the Peregrine solution (33), see examples in figures 13(b) and 14(b).

5. Conclusions

In this paper, we studied the integrable turbulence generated from the MI of the dn-branch of cnoidal waves. The corresponding problem of MI essentially depends on one free parameter, and the ratio ω_1/ω_0 between the imaginary and real half-periods of the cnoidal wave can be used as such. Using the scaling transformations, we fixed $\omega_0 = \pi$ and studied the dependence of integrable turbulence on the imaginary half-period ω_1 .

We found that the properties of the integrable turbulence change gradually with ω_1 , so that cnoidal waves with ‘intermediate’ ω_1 lead to turbulence with ‘intermediate’ properties between the two limits $\omega_1 \rightarrow 0$ and $\omega_1 \rightarrow +\infty$. Our results show, that in the nonlinear stage of the MI, the statistical characteristics of the turbulence evolve with time in an oscillatory way, approaching their asymptotics at late times. This means that the system asymptotically approaches the stationary state of the integrable turbulence in an oscillatory way. This state depends on cnoidal wave parameters and is defined by an infinite series of invariants (17) and (18).

During the evolution toward the asymptotic state, kinetic $\langle H_d(t) \rangle$ and potential $\langle H_4(t) \rangle$ energies, and also the moments $M^{(n)}(t)$, oscillate around their asymptotic values according to the ansatz (29). The amplitudes of these oscillations decay with time as $t^{-\alpha}$, with different exponents $1 < \alpha < 1.5$ for different cnoidal waves and moments $M^{(n)}(t)$. The oscillations are very small for cnoidal waves with small ω_1 , and pronounced for cnoidal waves with large ω_1 . The phases of the oscillations contain nonlinear phase shift decaying with time as $t^{-1/2}$, and the frequency is equal to the double maximal growth rate of the MI, $s = 2\gamma_{\max}$. Thus, for cnoidal waves with small ω_1 the frequency of the oscillations s is exponentially small and the oscillations themselves are very small too; for large ω_1 the oscillations are pronounced and their frequency approaches $s = 1$. The ratio of potential to kinetic energy in the asymptotic state is

equal to $Q_A = \langle H_4 \rangle / \langle H_d \rangle = -2$ for all cnoidal waves of the dn-branch, while the initial energy ratio is different $Q(0) \in (-\infty, -2)$ for different cnoidal waves. The other characteristics of turbulence—i.e. the wave-action spectrum, the spatial correlation function and the PDF—evolve with time in an oscillatory way coherently with kinetic and potential energies. We describe their evolution using points in time when the potential energy modulus $|\langle H_4(t) \rangle|$ takes maximal and minimal values; at these points the evolution of the spectrum, the correlation function and the PDF turn roughly to the opposite.

For unperturbed cnoidal waves (11) with $\omega_0 = \pi$, the wave-action spectrum represents a collection of peaks at integer wavenumbers $k_0 \in \mathbb{Z}$, and the spatial correlation function is periodic with period 2π . In the linear stage of the MI, the wave-action spectrum starts to rise most notably near the half-integer wavenumbers $k_0 + 1/2$, while the spatial correlation function does not change visibly. In the nonlinear stage and at the local maximums of $|\langle H_4(t) \rangle|$, the peaks in the spectrum at k_0 are smallest and the rest of the spectrum is maximally excited, while the correlation function takes (locally in time) minimal values at $|x| > 0$. At the local minimums of $|\langle H_4(t) \rangle|$, the peaks in the spectrum are largest and the rest of the spectrum is minimally excited, while the correlation function takes (locally in time) maximal values at $|x| > 0$. Thus, during the evolution toward the asymptotic state, the wave action is being ‘pumped’ in an oscillatory way between the peaks at integer wavenumbers and the rest of the spectrum, while the spatial correlation function ‘forms’ its tails at large lengths x .

The asymptotic wave-action spectrum decays exponentially $S_k \propto e^{-\rho|k|}$ at large k . The exponent ρ increases with ω_1 , so that for larger ω_1 the spectrum is narrower. For cnoidal waves with large ω_1 only the peak at the zeroth harmonic ‘survives’ in the asymptotic spectrum, while for small ω_1 many of the peaks at integer wavenumbers remain. Contrary to the original cnoidal wave, these peaks in the asymptotic spectrum do not occupy single harmonics k_0 only, but small regions of modes around k_0 where the spectrum behaves by a power law $S_k \propto |k - k_0|^{-\beta}$, $\beta > 0$, with different exponents β for different cnoidal waves and peaks $|k_0|$. These power-law peaks contain about 40% of all wave action $\langle N \rangle$, for all the cnoidal waves that we studied. For sufficiently large ω_1 most of this wave action is concentrated in quasi-condensate modes $|k| \leq \delta k$, $\delta k \sim 0.1$, which have extremely large scales $\ell \gg 2\pi$ in physical space. For small ω_1 , the quasi-condensate is replaced by the ‘quasi-cnoidal wave’—a collection of power-law peaks at the same positions where the peaks of the original cnoidal wave were situated.

The asymptotic spatial correlation function is close to Gaussian (30) at small lengths $|x| < x_{\text{corr}}/2$; its full width at half maximum x_{corr} increases with ω_1 so that for larger ω_1 the correlation function is wider. For sufficiently small ω_1 the asymptotic correlation function decays at large $|x|$ in an oscillatory way; these oscillations with period 2π are connected to the peaks at nonzero integer wavenumbers $|k_0| > 0$ in the asymptotic spectrum. We think that the amplitude of these oscillations decays with $|x|$ exponentially as in figure 10(b). For large ω_1 both the peaks in the asymptotic spectrum and the oscillations of the asymptotic correlation function disappear, and the correlation function decay is inversely proportional $g(x) \propto |x|^{-1}$ with $|x|$, as for the condensate case [7].

After the development of the MI from cnoidal waves with small ω_1 , the wave field remains close to a collection of singular solitons (6) with different phases and positions at all times. Moreover, the positions of these solitons remain generally very close to the positions of the ‘solitons’ of the original cnoidal wave. Thus, integrable turbulence transforms into the integrable soliton turbulence of very thin and high solitons (6). The amplitude of these solitons is already significantly larger than the mean amplitude $\langle |\Psi|^2 \rangle^{1/2}$. In the asymptotic stationary state of this turbulence, the PDF of the wave intensity is significantly non-exponential, and the dynamics of the system reduce to two-soliton collisions. These collisions provide up to a

two-fold increase in amplitude compared with the original cnoidal wave and occur at an exponentially small rate $\propto e^{-\pi\omega_0/\omega_1}$. Still, the probability of the occurrence of large waves during these collisions is much larger than it would be for an exponential PDF (2) with the same mean square amplitude $\sigma^2 = \langle |\Psi|^2 \rangle$. The potential to kinetic energy ratio $Q(t)$ for such turbulence at all times remains very close to -2 , as for the singular soliton (6).

Integrable turbulence generated from cnoidal waves with sufficiently large ω_1 is qualitatively and quantitatively very similar to that for the condensate case [7]. The PDF of this turbulence in the asymptotic state is exponential. During the evolution toward the asymptotic state, the PDF may significantly deviate from the exponential PDF; however, it does not exceed the exponential PDF by more than several times at any time.

Overall, for $\omega_1 \gtrsim 1.5$ the probability of the appearance of rogue waves does not exceed that for the exponential PDF significantly. For $\omega_1 \lesssim 1.5$, rogue waves may appear much more frequently than predicted by the exponential PDF, however the amplitude of these waves almost never exceeds the double maximal amplitude of the original cnoidal wave.

According to our observations, all sufficiently large waves that appear after the development of the MI at the time of their maximal elevation have a quasi-rational profile similar to that of the Peregrine solution of the NLS equation (32). We would like to stress that this similarity is not a sign that the Peregrine solution emerges in the problem of the MI of cnoidal waves, but is merely a characteristic of the spatial profile of the rogue waves. In the terminology of [35], the rogue waves that we observe could be the ‘concentrated’ cnoidal rogue wave or the ‘fused’ second-order cnoidal rogue wave. However, there is also another possibility that the observed rogue waves were formed from the collisions of breathers, which decomposed from ‘superregular’ solitonic solutions on the background of the cnoidal wave [36], similar to that in the condensate case [37, 38]. For sufficiently small ω_1 , solutions that describe the formation of rogue waves should transform into the collisions of singular solitons (6). It is interesting that for the first several extremums of the potential energy modulus, the phases of the rogue waves are close to $\arg \Psi \approx \pi/2 + \pi(m-1)$ for local maximums and $\arg \Psi \approx \pi + \pi(m-1)$ for local minimums of $|\langle H_4(t) \rangle|$, where m is the local maximum or local minimum index number respectively. We plan to examine the question of the origin of rogue waves in more detail in another publication.

The MI of the cn-branch of cnoidal waves (5) should lead to integrable turbulence with many similar properties. In particular, we expect similar oscillatory evolution for the characteristics of turbulence toward their asymptotics at late times. It is possible, though, that oscillations of the moments and also kinetic and potential energies are not described by the ansatz (29) exactly. We think that in the limit $\omega_1 \rightarrow 0$ both branches of cnoidal waves should lead to quantitatively similar stationary states, since in this limit integrable turbulence should transform into integrable soliton turbulence of very thin and high solitons (6).

However, for the cn-branch some properties of the integrable turbulence should be different. For instance, we expect that cnoidal waves (5) with large ω_1 will lead to almost linear integrable turbulence with a very small asymptotic potential to kinetic energy ratio $|Q_A| \ll 1$, since these cnoidal waves are close to the sinusoidal wave with an exponentially small amplitude (9). Therefore, for the cn-branch the asymptotic energy ratio Q_A should not be fixed to -2 , but should instead vary from $Q_A \rightarrow -2$ for $\omega_1 \rightarrow 0$ to $Q_A \rightarrow 0$ for $\omega_1 \rightarrow +\infty$. Our preliminary experiments confirm these suggestions. Note, that the initial energy ratio for the cn-branch of cnoidal waves is also limited in the same region $Q(0) \in (-2, 0)$. According to our observations, the study of the MI for the cn-branch of cnoidal waves is significantly more difficult than for the dn-branch, since development of the MI takes much more time and the subsequent oscillatory evolution toward the asymptotic stationary state is much slower too.

Combined with the studies [7, 8, 10] on condensate and incoherent wave initial conditions, this publication poses a series of questions concerning the general properties of integrable turbulence. Our results demonstrate that the turbulence generated from the MI of the dn-branch of cnoidal waves is quite similar to its limiting case $\omega_1 \rightarrow +\infty$, studied in [7] as the condensate initial conditions. In both cases, the turbulence approaches its asymptotic stationary state in an oscillatory way for a very long time. For incoherent initial wave conditions, the system reaches its stationary state very quickly [8, 10]. So what specifically in the initial conditions leads to such a dramatic difference in the time of arrival to the stationary state?

The oscillatory evolution of integrable turbulence for cnoidal wave initial conditions might be connected to the excitation of some multi-phase solutions of the NLS equation during the linear stage of the MI. This would explain why the frequency of the oscillations is equal to its double maximal growth rate. If true, then what are these multi-phase solutions? During our studies we also observed another interesting phenomenon: that the potential to kinetic energy ratio in the asymptotic stationary state is limited as $Q_A \in [-2, 0]$ (this ratio is equal to -2 for the dn-branch, and should be between -2 and 0 for the cn-branch of cnoidal waves). This raises the question of whether the asymptotic potential energy may exceed the kinetic energy by more than twice the amount, and if not, then what is the nature of the constrain? We plan to continue our studies of integrable turbulence in future publications.

Acknowledgments

The authors thank E Kuznetsov for valuable discussions concerning this publication, M Fedoruk for access to and V Kalyuzhny for assistance with the Novosibirsk Supercomputer Center. The work of VEZ was supported by RSF grant no. 14-22-00174 ‘Wave turbulence: theory, numerical simulation, experiment’, while the work of DSA was supported by RSF grant no. 14-50-00095 ‘The world ocean in the XXI century: climate, ecosystems, resources, natural disasters’.

Appendix A. Cnoidal waves

The cnoidal waves of real ω_0 and imaginary ω_1 half-periods have the general form [22]

$$\psi(x, t) = \sqrt{2} \frac{\sigma(x + i\omega_1 + a)}{\sigma(x + i\omega_1)\sigma(a)} e^{i\Omega t - \zeta(a)x - a\zeta(i\omega_1)}, \tag{A.1}$$

and are the exact periodic solutions of the NLS equation (3). Here, $\Omega = 3\wp(a)$, where a corresponds to one of the two possible branches of cnoidal waves $a = \omega_0$ (dn-branch) or $a = \omega_0 + i\omega_1$ (cn-branch), $\wp(z)$ is the Weierstrass elliptic function defined on the complex plane $z \in \mathbb{C}$ and is periodic along both the real and imaginary axes with periods $2\omega_0$ and $2\omega_1$ respectively, while $\sigma(z)$ and $\zeta(z)$ are the auxiliary Weierstrass sigma- and zeta-functions defined as $\zeta'(z) = -\wp(z)$ and $\sigma'(z)/\sigma(z) = \zeta(z)$. The dn- and cn-branches of the cnoidal waves can be rewritten as equations (4) and (5) respectively. In these equations $\nu = (e_1 - e_3)^{1/2}$, $s = (e_2 - e_3)^{1/2}/\nu$, and $e_1 > e_2 > e_3$ are values of $\wp(z)$ at $z = \omega_0$, $z = \omega_0 + i\omega_1$ and $z = i\omega_1$ respectively.

The square amplitude for both branches of cnoidal waves $a = \omega_0$ and $a = \omega_0 + i\omega_1$ is equal to [22]

$$|\psi(x, t)|^2 = 2\wp(a) - 2\wp(x + i\omega_1). \tag{A.2}$$

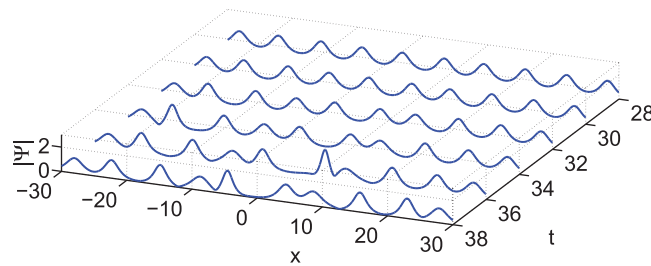


Figure B1. The development of the MI on the background of a cnoidal wave with $\omega_0 = \pi$, $\omega_1 = 1.6$. Significant perturbations in amplitude $|\Psi|$ become visible starting from $t = 32$; compare with figure 2(a).

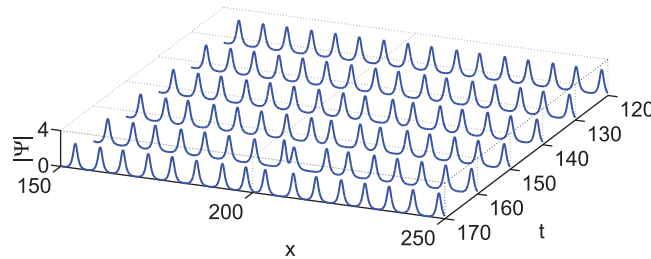


Figure B2. The development of the MI on the background of a cnoidal wave with $\omega_0 = \pi$, $\omega_1 = 0.8$. Significant perturbations in amplitude $|\Psi|$ become visible starting from $t = 140$; compare with figure 17(a).

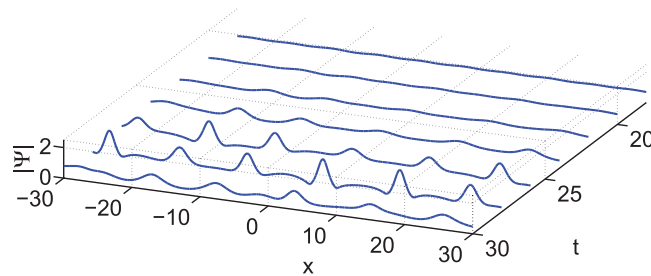


Figure B3. The development of the MI on the background of a cnoidal wave with $\omega_0 = \pi$, $\omega_1 = 5$. Significant perturbations in amplitude $|\Psi|$ become visible starting from $t = 22$; compare with figure 17(b).

The weierstrass function $\wp(z)$ has a representation in the form of an infinite series of KdV-solitons [40]

$$-2 \wp(x + i\omega_1) = \frac{\zeta(i\omega_1)}{i\omega_1} + \sum_{m=-\infty}^{+\infty} \frac{2\lambda^2}{\cosh^2 \lambda(x - 2m\omega_0)}, \quad \lambda = \pi/2\omega_1. \quad (\text{A.3})$$

Note, that the square root of the KdV-soliton gives a soliton solution (6) for the NLS equation (3). Thus, one can say that cnoidal waves represent infinite lattices of overlapping solitons, with the width of the solitons proportional to ω_1 and the distance between them equal to $2\omega_0$.

Appendix B. Development of the MI on the cnoidal wave background

In this appendix we demonstrate how the MI develops on the background of three cnoidal waves with $\omega_1 = 0.8$ (weak overlapping), $\omega_1 = 1.6$ (moderate overlapping) and $\omega_1 = 5$ (strong overlapping). We consider one realization of initial noise for each of these cnoidal waves.

References

- [1] Mussot A, Kudlinski A, Kolobov M, Louvergneaux E, Douay M and Taki M 2009 *Opt. Express* **17** 17010–5
- [2] Genty G, De Sterke C M, Bang O, Dias F, Akhmediev N and Dudley J M 2010 *Phys. Lett. A* **374** 989–96
- [3] Taki M, Mussot A, Kudlinski A, Louvergneaux E, Kolobov M and Douay M 2010 *Phys. Lett. A* **374** 691–5
- [4] Hammani K, Kibler B, Finot C and Picozzi A 2010 *Phys. Lett. A* **374** 3585–9
- [5] Chung Y and Lushnikov P M 2011 *Phys. Rev. E* **84** 036602
- [6] Randoux S, Walczak P, Onorato M and Suret P 2014 *Phys. Rev. Lett.* **113** 113902
- [7] Agafontsev D S and Zakharov V E 2015 *Nonlinearity* **28** 2791–821
- [8] Walczak P, Randoux S and Suret P 2015 *Phys. Rev. Lett.* **114** 143903
- [9] Agafontsev D S and Zakharov V E 2015 *Phys. Lett. A* **379** 2586–90
- [10] Suret P, El Koussaifi R, Tikan A, Evain C, Randoux S, Szewaj C and Bielawski S 2016 arXiv:1603.01477
- [11] Solli D R, Ropers C, Koonath P and Jalali B 2007 *Nature* **450** 1054–7
- [12] Kharif C and Pelinovsky E 2003 *Eur. J. Mech. B* **22** 603–34
- [13] Dysthe K, Krogstad H E and Muller P 2008 *Annu. Rev. Fluid Mech.* **40** 287–310
- [14] Onorato M, Residori S, Bortolozzo U, Montina A and Arecchi F T 2013 *Phys. Rep.* **528** 47–89
- [15] Nazarenko S 2011 *Wave Turbulence* vol 825 (Berlin: Springer)
- [16] Zakharov V E 2009 *Stud. Appl. Math.* **122** 219–34
- [17] Suret P, Picozzi A and Randoux S 2011 *Opt. Express* **19** 17852–63
- [18] Picozzi A, Garnier J, Hansson T, Suret P, Randoux S, Millot G and Christodoulides D N 2014 *Phys. Rep.* **542** 1–132
- [19] Onorato M, Osborne A R, Serio M and Damiani T 2000 *Rogue Wave 2000* (Versailles Cedex: QUAE) p 181
- [20] Onorato M, Osborne A R, Serio M, Cavaleri L, Brandini C and Stansberg C T 2004 *Phys. Rev. E* **70** 067302
- [21] Onorato M, Osborne A R, Serio M, Cavaleri L, Brandini C and Stansberg C T 2006 *Eur. J. Mech. B* **25** 586–601
- [22] Kuznetsov E A and Spector M D 1999 *Teor. Mat. Fyz.* **120** 997–1008
- [23] Ma Y C and Ablowitz M J 1981 *Stud. Appl. Math.* **65** 113–58
- [24] Zakharov V E, Manakov S V, Novikov S P and Pitaevsky L P 1984 *Theory of Solitons: the Inverse Scattering Method* (Berlin: Springer)
- [25] Belokolos E D and Bobenko A I 1994 *Algebro-Geometric Approach to Nonlinear Integrable Equations* (Springer Verlag)
- [26] Zakharov V E, Pushkarev A N, Shvets V F and Yankov V V 1988 *Pis'ma Zh. Eksp. Teor. Fiz.* **48** 79–82
- [27] Dyachenko A I, Zakharov V E, Pushkarev A N, Shvets V F and Yankov V V 1989 *Zh. Eksp. Teor. Fiz.* **96** 2026
- [28] Mamyshev P V, Chernikov S V and Dianov E M 1991 *Quantum Electron.* **27** 2347–55
- [29] Haus H A and Wong W S 1996 *Rev. Mod. Phys.* **68** 423
- [30] Onorato M, Proment D, El G, Randoux S and Suret P 2016 *Phys. Lett. A* **380** 3173–7
- [31] Peregrine D H 1983 *J. Aust. Math. Soc. B* **25** 16–43
- [32] Kibler B, Fatome J, Finot C, Millot G, Dias F, Genty G, Akhmediev N and Dudley J M 2010 *Nat. Phys.* **6** 790–5
- [33] Fermi E, Pasta J and Ulam S 1955 *Los Alamos Report LA-1940* pp 978–88
- [34] Infeld E 1981 *Phys. Rev. Lett.* **47** 717

- [35] Kedziora D J, Ankiewicz A and Akhmediev N 2014 *Eur. Phys. J. Spec. Top.* **223** 43–62
- [36] Gelash A A 2015 private communication
- [37] Gelash A A and Zakharov V E 2014 *Nonlinearity* **27** R1
- [38] Kibler B, Chabchoub A, Gelash A A, Akhmediev N and Zakharov V E 2015 *Phys. Rev. X* **5** 041026
- [39] Akhmediev N, Soto-Crespo J M and Ankiewicz A 2009 *Phys. Lett. A* **373** 2137–45
- [40] Kuznetsov E A and Mikhailov A V 1974 *Zh. Eksp. Teor. Fiz.* **67** 1717–27